The mitochondrial citrate carrier SLC25A1 regulates metabolic reprogramming and morphogenesis in the developing heart

Check for updates

Chiemela Ohanele[1,2], Jessica N. Peoples[2], Anja Karlstaedt [3], Joshua T. Geiger[4], Ashley D. Gayle[2], Nasab Ghazal [1,2], Fateemaa Sohani[2], Milton E. Brown[5], Michael E. Davis[5], George A. Porter Jr. [6], Victor Faundez[7] & Jennifer Q. Kwong [2,7] ✉

The developing mammalian heart undergoes an important metabolic shift from glycolysis towards mitochondrial oxidation that is critical to support the increasing energetic demands of the maturing heart. Here, we describe a new mechanistic link between mitochondria and cardiac morphogenesis, uncovered by studying mitochondrial citrate carrier (SLC25A1) knockout mice. *Slc25a1* null embryos displayed impaired growth, mitochondrial dysfunction and cardiac malformations that recapitulate the congenital heart defects observed in 22q11.2 deletion syndrome, a microdeletion disorder involving the *SLC25A1* locus. Importantly, *Slc25a1* heterozygous embryos, while overtly indistinguishable from wild type, exhibited an increased frequency of these defects, suggesting *Slc25a1* haploinsuffiency and dose-dependent effects. Mechanistically, SLC25A1 may link mitochondria to transcriptional regulation of metabolism through epigenetic control of gene expression to promote metabolic remodeling in the developing heart. Collectively, this work positions SLC25A1 as a novel mitochondrial regulator of cardiac morphogenesis and metabolic maturation, and suggests a role in congenital heart disease.

In the postnatal heart, mitochondria drive metabolism, providing oxidative energy for contraction. However, the prenatal heart is a hypoxic environment[1] with unresolved roles for mitochondrial oxidative energy systems. Nonetheless, mitochondrial metabolism is critical for embryogenesis, as defects in respiratory chain regulation result in lethality by embryonic (E) day 10.5 (E10.5)[2–6]. Before E11.5, cardiac mitochondria are immature and rely mainly on glycolysis for ATP. As development proceeds (E14.5), cardiac mitochondria mature, and metabolism shifts toward mitochondrial oxidation[7,8]. This transition may support the increasing energetic demands of the developing heart since increased oxidative metabolism is a cornerstone of cardiomyocyte maturation[9].

In parallel with this embryonic metabolic shift, the developing heart undergoes ventricular wall maturation with key processes being trabeculation, septation, and compaction[10,11]. While metabolism and ventricular morphogenesis are seemingly disparate processes, human primary mitochondrial disorders offers insight into the connection between energetics and ventricular morphogenesis. Patients with mitochondrial disorders including Barth syndrome, MELAS (mitochondrial encephalopathy, lactic acidosis, and stroke-like episodes), and MERRF (myoclonic epilepsy with ragged-red fibers) can present with left ventricular noncompaction, a congenital heart defect caused by impaired compaction of the ventricular wall, suggesting an association between mitochondrial energetics and cardiac structural malformations[12,13]. However, the molecular mechanisms connecting energetics to ventricular wall morphogenesis are not fully understood. Defining these connections may inform the biology of cardiac development and highlight new targets for improved interventions for congenital heart disease (CHD).

One possible connection between mitochondrial energetics and other cellular processes is the mitochondrial citrate carrier SLC25A1. SLC25A1 is an inner membrane transporter that exports citrate out of the mitochondrial

---

[1]Graduate Program in Biochemistry, Cell and Developmental Biology; Graduate Division of Biological and Biomedical Sciences; Emory University, Atlanta, GA, USA. [2]Division of Pediatric Cardiology; Department of Pediatrics; Emory University School of Medicine; and Children's Healthcare of Atlanta, Atlanta, GA, USA. [3]Department of Cardiology; Smidt Heart Institute; Cedars-Sinai Medical Center, Los Angeles, CA, USA. [4]Division of Vascular Surgery; University of Rochester Medical Center, Rochester, NY, USA. [5]Wallace H. Coulter Department of Biomedical Engineering; Emory University School of Medicine, Atlanta, GA, USA. [6]Department of Pediatrics; Division of Cardiology; University of Rochester Medical Center, Rochester, NY, USA. [7]Department of Cell Biology; Emory University School of Medicine, Atlanta, GA, USA. ✉e-mail: jennifer.kwong@emory.edu

matrix[14,15]. While mitochondrial citrate is a tricarboxylic acid (TCA) cycle intermediate central to oxidative metabolism, cytosolic citrate is converted into acetyl-CoA which is used in biological pathways ranging from lipid biosynthesis to protein post-translational acetylation and epigenetic control of gene expression[16–18].

Loss of SLC25A1 reduces respiratory chain function in vitro[19–21], suggesting that SLC25A1 may regulate mitochondrial function. The *SLC25A1* gene is located within a chromosome 22 region compromised in 22q11.2 deletion syndrome (22q11.2DS/DiGeorge syndrome). Hemizygous deletion of this region results in a multisyndromic disorder that includes congenital heart defects in approximately 60–80% of affected individuals[22,23]. We reported that the neurodevelopmental pathology of 22q11.2DS arises in part due to *SLC25A1* loss, which leads to mitochondrial dysfunction and dysregulation of mitochondrial proteins[24]. Collectively, these data indicate SLC25A1 is a mitochondrial protein that regulates mitochondrial function and connects mitochondria to cytosolic processes. However, the roles of SLC25A1, particularly during development, are not fully delineated.

Here we investigated the role of SLC25A1 in development using systemic *Slc25a1* knockout (KO) mice. Our findings implicate SLC25A1 in epigenetic regulation of metabolic reprogramming in the developing heart and positions SLC25A1 as a mitochondrial regulator of cardiac morphogenesis. Importantly, *Slc25a1* KO mouse model recapitulates cardiac defects in 22q11.2DS, providing important new insights for this disorder.

Results

Systemic *Slc25a1* deletion impairs embryonic growth and causes perinatal lethality

We used the *Slc25a1* KO mouse line developed by the International Mouse Phenotyping Consortium to model systemic deletion of *Slc25a1*[25], and to reflect systemic gene loss that would be observed in humans with SLC25A1 deficiencies. For these mice, the *Slc25a1* KO allele (*Slc25a1⁻*) was generated by insertion of an IRES:LacZ trapping cassette and a neomycin selection cassette between exons 1 and 2 of *Slc25a1* (Fig. 1A). *Slc25a1* KO mice (*Slc25a1⁻/⁻*) exhibit perinatal lethality [26]. Thus, we conducted timed matings of *Slc25a1* hemizygous KO mice (*Slc25a1⁺/⁻*) to study the effects of *Slc25a1* ablation (*Slc25a1⁻/⁻*) and *Slc25a1* hemizygous loss (*Slc25a1⁺/⁻*), compared with wild type (WT) littermate controls (*Slc25a1⁺/⁺*). We confirmed that *Slc25a1⁻/⁻* embryos at E18.5 were viable, and *Slc25a1⁺/⁻* intercrosses yielded the anticipated genotypic frequencies (Fig. 1G). However, E18.5 *Slc25a1⁻/⁻* embryos displayed impaired growth with reduced crown-rump lengths compared to *Slc25a1⁺/⁻* and *Slc25a1⁺/⁺* controls (Fig. 1B, C). Additionally, while *Slc25a1⁻/⁻* embryos displayed microencephaly, anencephaly, encephalocele, and gastroschisis, *Slc25a1⁺/⁻* embryos were indistinguishable from *Slc25a1⁺/⁺* controls. Analyses of SLC25A1 protein levels in E18.5 heart and brain revealed robust expression in *Slc25a1⁺/⁺* embryos, reduced expression in *Slc25a1⁺/⁻* embryos, and absent expression from *Slc25a1⁻/⁻* embryos (Fig. 1D). This gene dosage-dependent SLC25A1expression was confirmed by immunofluorescence in embryonic hearts. In WT E14.5 hearts, SLC25A1 strongly colocalizes with the mitochondrial inner membrane protein ATP5A1, confirming mitochondrial localization (Supplemental Fig. 1). However, while SLC25A1 immunofluorescence was robust in *Slc25a1⁺/⁺* hearts, expression was weaker in *Slc25a1⁺/⁻* hearts and undetectable in *Slc25a1⁻/⁻* hearts (Fig. 1E).

Consistent with previous reports, we were unable to recover adult *Slc25a1⁻/⁻* mice from *Slc25a1⁺/⁻* intercrosses. However, *Slc25a1⁻/⁻* pups were born and obtained at the anticipated genotype frequencies (Fig. 1F, G). Further, postnatal (P) day 0 (P0) *Slc25a1⁻/⁻* neonates were small and cyanotic, and some displayed microencephaly and gastroschisis (Fig. 1F). Importantly, *Slc25a1⁻/⁻* neonates died within 6 h of birth, suggesting that systemic *Slc25a1* ablation causes perinatal lethality.

Partial *Slc25a1* deletion is sufficient to produce cardiac structural defects in mice

SLC25A1 is expressed in the mouse heart[27,28], and given that *Slc25a1⁻/⁻* neonates were cyanotic, we hypothesized that SLC25A1 loss could impair cardiac contractile function. We assessed SLC25A1 expression in the developing heart by immunofluorescence in WT E10.5, E12.5, and E14.5 embryos and E18.5 hearts. Because the cardiac endocardium, myocardium, and epicardium play distinct roles in ventricular morphogenesis, we investigated expression of SLC25A1 in these different layers. Examining fields of the embryonic heart spanning the myocardium and epicardium (Fig. 2A) as well as the myocardium and endocardium (Supplemental Fig. 2), we observed strong SLC25A1 expression in the myocardium and epicardium (Fig. 2A) and minimal expression in the endocardium (Supplemental Fig. 2).

To investigate the structural consequences of SLC25A1 loss in the embryonic heart, we obtained *Slc25a1⁻/⁻*, *Slc25a1⁺/⁻*, and control *Slc25a1⁺/⁺* embryos from intercrosses of *Slc25a1⁺/⁻* mice. Embryos were collected at E10.5, E12.5, and E14.5 and hearts were collected at E18.5 to reflect timepoints when trabeculation occurs (E10.5 and E12.5), when septation should be complete and ventricular wall compaction should be fulminant (E14.5), and when major embryonic milestones of cardiac morphogenesis should be complete (E18.5)[10,11]. Histological analyses revealed similar cardiac morphology in E10.5 *Slc25a1⁺/⁺, Slc25a1⁺/⁻, and Slc25a1⁻/⁻* embryos (Fig. 2B). At E12.5, the compact myocardium of *Slc25a1⁻/⁻* embryos appeared to be slightly less developed than that of *Slc25a1⁺/⁺* and *Slc25a1⁺/⁻* embryos (Fig. 2C). However, by E14.5 and E18.5, hearts from *Slc25a1⁻/⁻* embryos displayed cardiac abnormalities (Fig. 2D–H) including ventricular septal defects (VSDs); ventricular noncompaction, as evidenced by decreased compact myocardium and increased trabecular myocardium (Fig. 2F, G) compared to age-matched *Slc25a1⁺/⁺* controls; and right ventricular hypoplasia. As VSDs have been reported in *Slc25a1⁻/⁻* embryos[29], our findings extend the cardiac abnormalities associated with *Slc25a1* deletion to include noncompaction and right ventricular hypoplasia.

Slc25a1⁺/⁻ embryos, which were morphologically indistinguishable from *Slc25a1⁺/⁺* controls, unexpectedly displayed increased frequency of cardiac malformations including VSDs, ventricular noncompaction, and right ventricular hypoplasia (Fig. 2D–H). Collectively, our data demonstrate that SLC25A1 is necessary for ventricular morphogenesis and that heterozygous loss (*Slc25a1* haploinsufficiency) is sufficient to cause structural defects in the developing heart.

Slc25a1 haploinsufficiency decreases neonatal survival in mice

While *Slc25a1⁺/⁻* embryos displayed congenital heart defects, adult *Slc25a1⁺/⁻* mice were fertile and did not display differences in survival with aging. This prompted us to investigate the structural and functional consequences of *Slc25a1* haploinsufficiency in the postnatal heart, and specifically, if adult *Slc25a1⁺/⁻* mice harbor cardiac defects. Histological analyses of hearts from 2-month-old *Slc25a1⁺/⁻* and *Slc25a1⁺/⁺* control mice (n = 10/ group) revealed no structural or morphological defects (Supplemental Fig. 3A). Additionally, no changes were observed in gravimetric or echocardiographic parameters (Supplemental Fig. 3B, C), suggesting that cardiac structure and function were unaltered in adult *Slc25a1⁺/⁻* mice.
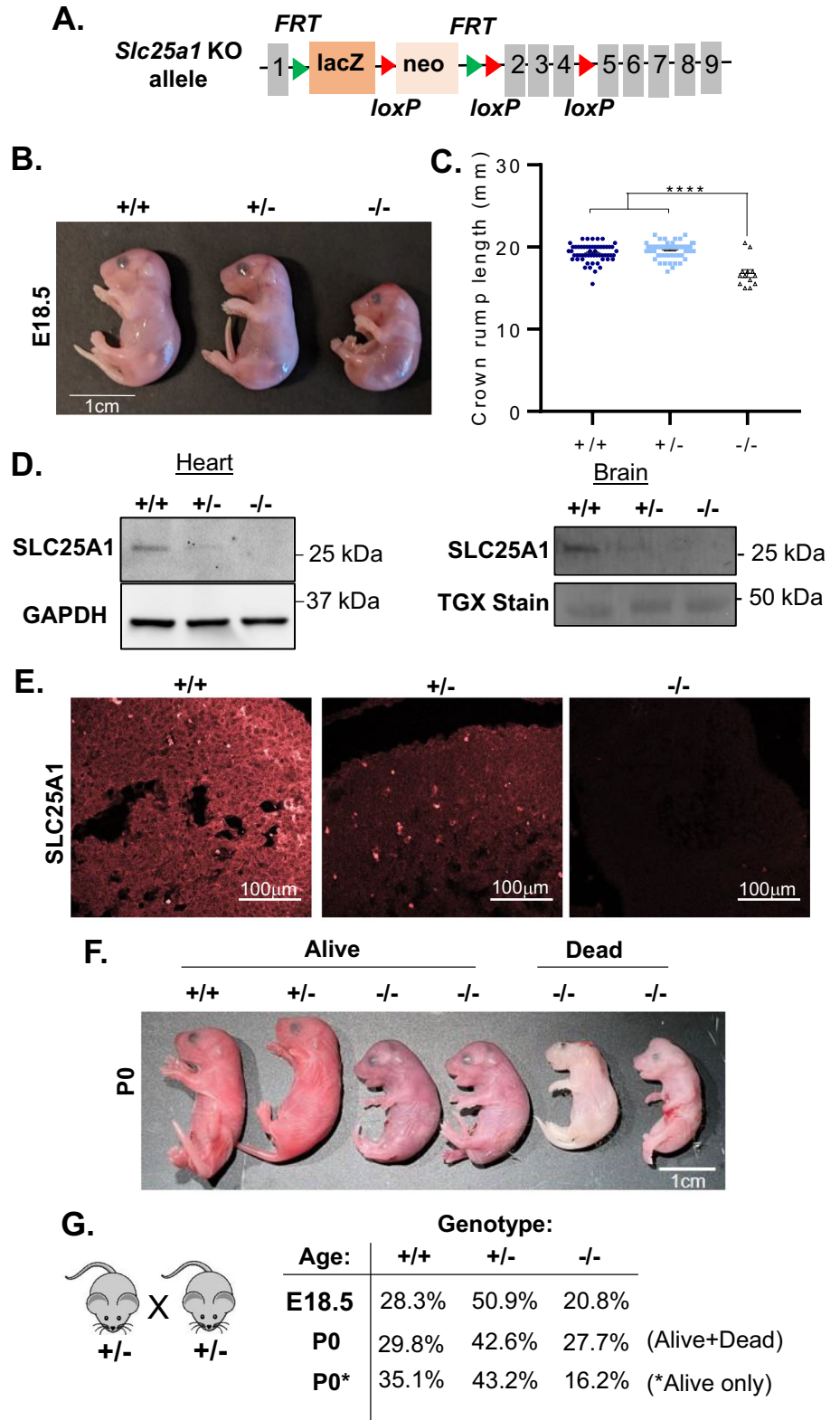
To understand how we could observe cardiac malformations in *Slc25a1⁺/⁻* embryos but not adult mice, we examined the frequencies of progeny genotypes. We used a breeding strategy of *Slc25a1⁺/⁻* mice crossed to *Slc25a1⁺/⁺* mice, with genotyping conducted on P7 tissue biopsies. Genotype analyses of 446 pups from 80 litters revealed a slight but significant [χ^2 (1, N = 446) = 6.0628; p = 0.014] increase in the frequency of P7 *Slc25a1⁺/⁺* (56% observed; 50% expected) versus *Slc25a1⁺/⁻* pups obtained (44% observed; 50% expected; Supplemental Fig. 3D), even though *Slc25a1⁺/⁻* pups were recovered at expected frequencies at P0 (N = 47, Fig. 1F). These data suggest that *Slc25a1* haploinsufficiency decreases neonatal survival. Moreover, as cardiac morphometry and function in *Slc25a1⁺/⁻* mice were normal at 2 months of age, our data suggest that *Slc25a1⁺/⁻* pups born with cardiac defects die in the neonatal period.

Association analysis of SLC251A variants and pediatric CHD

In humans, *SLC25A1* single-gene variants underlie two rare neurometabolic and neuromuscular diseases, D-2 and L-2 aciduria (DL-2HGA;

Fig. 1 | Systemic *Slc25a1* deletion impairs mouse embryonic growth and causes perinatal lethality.
A Schematic of the *Slc25a1* knockout (KO) first allele. A lacZ-neo KO cassette was inserted between exons 1 and 2 of *Slc25a1*. **B** Representative E18.5 *Slc25a1*^{+/+}, *Slc25a1*^{+/-}, and *Slc25a1*^{-/-} embryos obtained from timed intercross of *Slc25a1*^{+/-} mice. **C** Quantification of crown-rump lengths of E18.5 embryos of the indicated genotypes (*n* = 13–26/group). Values reported as mean ± SEM. One-tailed Student's *t* test was used for statistical analysis. ****$P < 0.0001$. **D** Western blot of SLC25A1 expression in total protein isolated from E17.5 hearts and brains from the indicated genotypes. GAPDH or TGX protein staining was used as loading controls. **E** Representative immuno-fluorescence images of SLC25A1 expression in E14.5 hearts from the indicated genotypes.
F Representative image of P0 pups obtained from timed intercross of *Slc25a1*^{+/-} mice. **G** Genotype frequencies of E18.5 embryos and P0 pups obtained from timed intercross of *Slc25a1*^{+/-} mice. Illustrations from Clkr.com.

Age:	Genotype:		
	+/+	+/-	-/-
E18.5	28.3%	50.9%	20.8%
P0	29.8%	42.6%	27.7% (Alive+Dead)
P0*	35.1%	43.2%	16.2% (*Alive only)

OMIM: 615182) and congenital myasthenic syndrome-23 (CMS23; OMIM: 618197)[30–32]. *SLC25A1* also is among the genes lost in the chromosomal microdeletion disorder 22q11.2DS (OMIM:188400)[22,33]. Individuals with 22q11.2DS can present with CHD, but these defects have not been attributed to *SLC25A1*[33]. Additionally, there are no human cardiac phenotypes annotated to *SLC25A1* single-gene defects (https://hpo.jax.org/app/browse/gene/6576), and it is unknown if *SLC25A1* variants underlie cardiac disease. Yet, our surprising findings of ventricular malformations in *Slc25a1*

deficient mouse embryos prompted us to investigate if *SLC25A1* variants are associated with human CHD. We analyzed whole-exome sequencing data from the Pediatric Cardiac Genomics Consortium (PCGC), encompassing 3740 CHD probands with 3401 pseudo-sibship case-controlled pairs (generated from parent-proband trios)[34,35]. Rare *SLC25A1* variants were selected using a minor allele frequency of <0.001 in the Genome Aggregation Database (gnomAD) and a combined annotation-dependent depletion (CADD) score of >20. We generated a separate set including only ultrarare
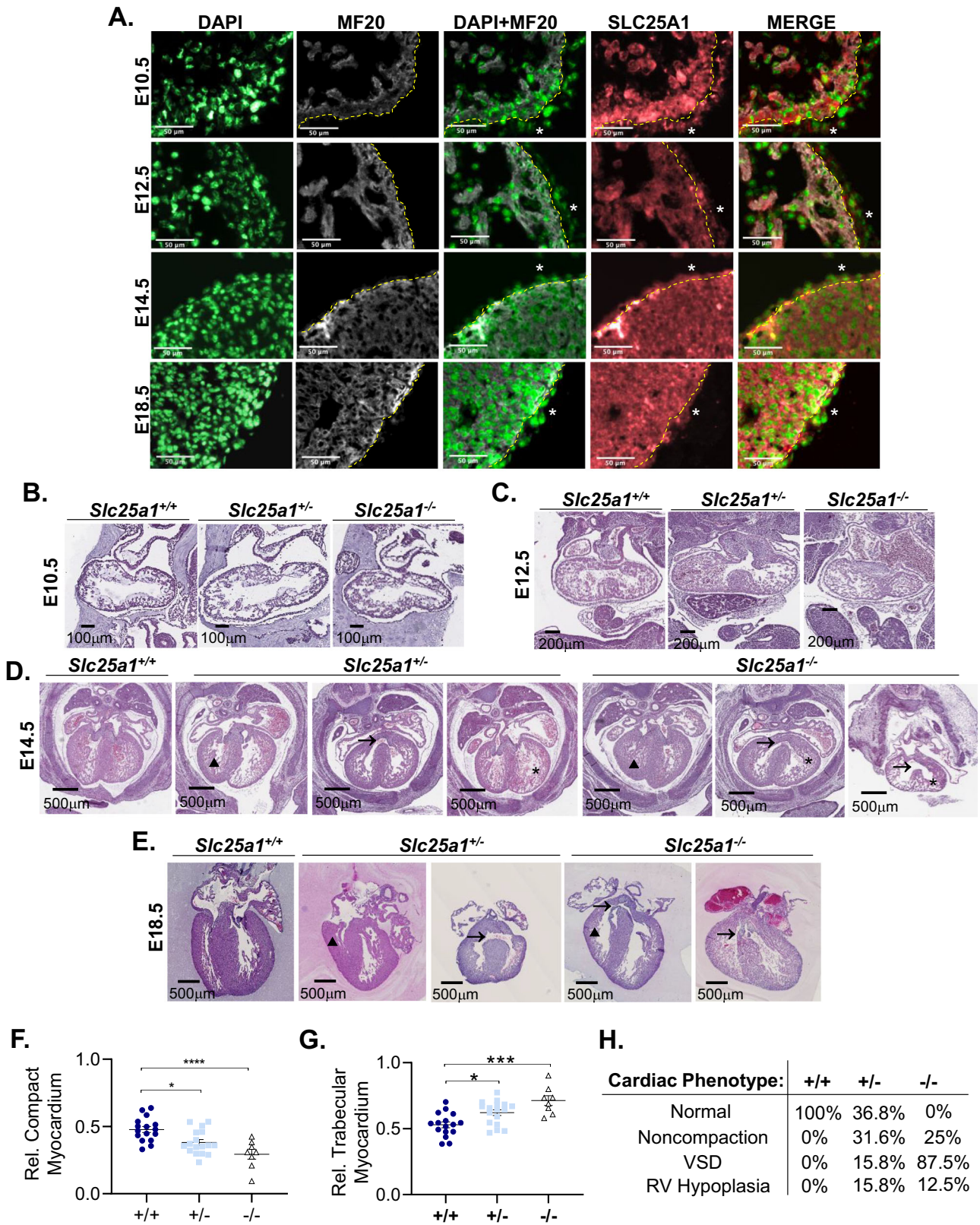
Fig. 2 | Partial *Slc25a1* deletion is sufficient to produce cardiac structural defects in mice. **A** Representative immunofluorescence images of SLC25A1 expression in wild type embryo (E10.5, E12.5, and E14.5) and heart (E18.5) sections (6 μm). DAPI was used to counterstain nuclei, and MF20 was used to counterstain cardiomyocytes. Dashed yellow line outlines myocardium from the epicardium; asterisk indicates epicardium positive for SLC25A1. **B** Representative images of E10.5 embryos, (**C**) E12.5 embryos, (**D**) E14.5 embryos, and (**E**) E18.5 hearts from the indicated genotypes stained with hematoxylin and eosin. Asterisk indicates noncompaction, arrow indicates ventricular septal defect, and triangle indicates right ventricular hypoplasia. **F** Quantification of relative compact myocardium thickness or (**G**) relative trabecular myocardium thickness in E18.5 hearts ($n = 8$-17/group). **H** Frequency of cardiac defects observed at E14.5 in embryos with the indicated genotypes ($n = 27$/group). Values reported as mean ± SEM. One-tailed Student's t test was used for statistical analysis. $*P < 0.05$; $***P < 0.0005$; $****P < 0.0001$.
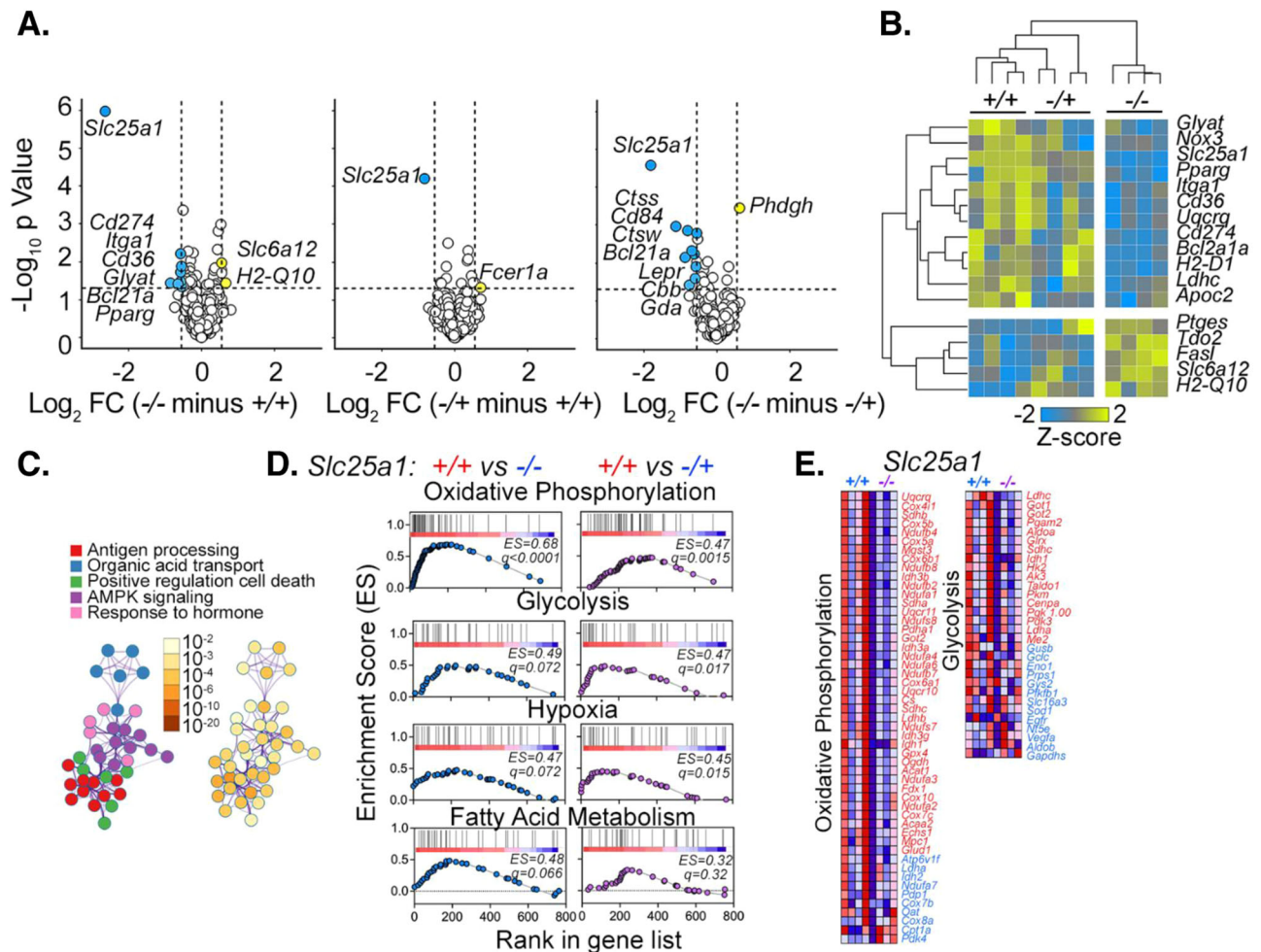
Fig. 3 | *Slc25a1* deletion alters metabolic gene expression in mice. A Volcano plots of Nanostring metabolic transcript profiling comparing gene expression of *Slc25a1*-/- and *Slc25a1*+/+, *Slc25a1*+/- and *Slc25a1*+/+, and *Slc25a1*-/- and Slc25a1+/- E17.5 hearts. Blue denotes downregulated transcripts. Yellow denotes upregulated transcripts. See Supplemental Data 3. **B** Heat map depicting transcripts differentially expressed across genotypes in A. Transcripts in rows were selected by ANOVA multiple comparisons followed by Benjamini-Hochberg correction ($q < 0.05$) and clustered using Kendall-Tau (see Supplemental Data 3). Each column represents an individual animal. **C** Gene ontologies identified with Metascape from genes differentially expressed in *Slc25a1*-/- and *Slc25a1*+/- versus *Slc25a1*+/+ hearts. **D** Geneset enrichment analysis of oxidative phosphorylation, glycolysis, hypoxia, and fatty acid metabolism genes in *Slc25a1*+/+ vs. *Slc25a1*-/- and *Slc25a1*+/+ vs. *Slc25a1*+/- E17.5 hearts. **E** Heatmaps visualizing gene expression of oxidative phosphorylation and glycolysis genes from Nanostring transcript profiling in E17.5 *Slc25a1*+/+ vs. *Slc25a1*-/- hearts. Blue denotes reduced expression; red denotes increased expression.

(i.e., do not appear in gnomAD exomes) and loss-of-function *SLC25A1* variants. While we were unable to identify an association of rare and ultrarare *SLC25A1* variants with specific CHD presentations, gene burden analyses using the kernel-based adaptive cluster (KBAC) method revealed that ultrarare nonsynonymous and stop-gain *SLC25A1* variants trend towards an association with CHD ($p = 0.058$ and Bonferroni-corrected *p*-value of 0.0167 ; Supplemental Data 1). Moreover, many of these variants were associated with cardiac defects including VSDs, tetralogy of Fallot, and conotruncal defects—which are observed in 22q11.2DS (Supplemental Data 2).

Slc25a1 deletion alters metabolic gene expression in mice
SLC25A1 functions as a mitochondrial solute transporter which exports mitochondrial citrate[14,15]. Previous studies have suggested a role for SLC25A1 beyond metabolite transport in the direct regulation of respiratory chain function, as SLC25A1 deletion in cancer and neuronal systems leads to impaired respiration[19,24,36]. Our work in the HAP1 human near-haploid lymphoblastoid cell line proposes a role for SLC25A1 in the regulation of mitochondrial translation, as loss of SLC25A1 is associated with reduced expression of core mitochondrial ribosome subunits[21]. Thus, we hypothesized that SLC25A1 regulation of mitochondrial translation and respiration

would also be operant in the developing heart. We examined expression levels of key mitochondrial ribosome subunits, MRPS22 and MRPS18B, in E17.5 *Slc25a1*+/+, *Slc25a1*+/-, and *Slc25a1*-/- embryonic hearts. Surprisingly, MRPS22 and MRPS18B expression was unchanged with *Slc25a1* deletion (Supplemental Fig. 4), suggesting that SLC25A1 does not regulate mitochondrial translation in the developing heart.

To delineate the metabolic consequences of *Slc25a1* deletion, we used a NanoString mRNA quantification panel to profile expression of 768 metabolism-related genes encompassing key metabolic pathways. Profiling metabolic gene expression in *Slc25a1*+/- versus *Slc25a1*+/+, *Slc25a1*-/- versus *Slc25a1*+/+, and *Slc25a1*+/- versus *Slc25a1*-/- hearts revealed 28 distinct differentially expressed genes (DEGs) with *Slc25a1* deletion at E17.5 ($p < 0.05$). Of these genes, 10 were differentially expressed between *Slc25a1*-/- versus *Slc25a1*+/+, two between *Slc25a1*+/- versus *Slc25a1*+/+, and 11 between *Slc25a1*+/- versus *Slc25a1*-/- hearts (fold-change = 1.5; $p < 0.05$; Fig. 3A). Hierarchical clustering of DEGs revealed that while *Slc25a1*+/+ and *Slc25a1*-/- hearts had distinct gene expression profiles, *Slc25a1*+/- hearts had an intermediate pattern (Fig. 3B), suggesting that SLC25A1 deletion-associated dysregulation of metabolic genes occurs in a dosage-dependent manner. Additionally, using Metascape[37] we identified antigen processing, organic acid transport, positive regulation of cell death, AMPK signaling, and

response to hormone as the most significantly altered pathways with *Slc25a1* deletion (Fig. 3C).

To define metabolic processes impacted by *Slc25a1* deletion, we performed gene set enrichment analysis (GSEA) of REACTOME pathways using normalized gene expression from the NanoString panel as gene ranks. GSEA revealed oxidative phosphorylation, glycolysis, hypoxia, and fatty acid metabolism as the most significantly altered pathways in *Slc25a1*⁻/⁻ versus *Slc25a1*⁺/⁺ and *Slc25a1*⁺/⁻ versus *Slc25a1*⁺/⁺ hearts, with higher enrichment scores for these pathways in control *Slc25a1*⁺/⁺ hearts versus hearts with *Slc25a1* deletion (*Slc25a1*⁻/⁻ and *Slc25a1*⁺/⁻) (Fig. 3D, E). These results suggest that *Slc25a1* deletion induces mitochondrial dysfunction and metabolic remodeling of the embryonic heart.

Importantly, these data show that loss of one copy of *Slc25a1* is sufficient to induce gene expression changes. Intriguingly, comparisons of the enrichment plots for oxidative phosphorylation, glycolysis, hypoxia, and fatty acid metabolism revealed a right-ward shift of the *Slc25a1*⁺/⁻ versus *Slc25a1*⁺/⁺ plots as compared to *Slc25a1*⁻/⁻ versus *Slc25a1*⁺/⁺ plots (Fig. 3D). These graded differences between homozygous and heterozygous *Slc25a1* knockouts suggest that full *Slc25a1* ablation induces greater mitochondrial and metabolic dysregulation than partial loss. These results align with our findings that *Slc25a1*⁻/⁻ embryos displayed a higher frequency and severity of ventricular malformations than *Slc25a1*⁺/⁻ embryos.

Slc25a1 deletion causes mitochondrial ultrastructural defects in embryonic mouse heart

Our metabolic gene expression profiling suggested that SLC25A1 loss causes dosage-dependent mitochondrial dysfunction in the developing heart. Because mitochondrial structure and function are often linked[38], we investigated the impact of SLC25A1 loss on mitochondrial ultrastructure. Transmission electron microscopy of E17.5 hearts revealed both partial and complete *Slc25a1* ablation induced striking alterations in cardiac mitochondrial morphology— highly immature mitochondria with disordered cristae and open matrix voids (Fig. 4A). Quantification of mitochondrial morphology further revealed that *Slc25a1*⁺/⁻ and *Slc25a1*⁻/⁻ mitochondria had significantly increased area and minimal Feret's diameter, despite similar circularity (Supplemental Fig. 5A–C), suggesting larger and swollen mitochondria. *Slc25a1*⁻/⁻ mitochondria further displayed significantly decreased aspect ratio (Supplemental Fig. 5D) and increased roundness (Supplemental Fig. 5E), suggesting that complete SLC25A1 ablation causes greater changes in mitochondrial morphology, compared to partial loss. Our data suggest that, similar to metabolic gene expression changes, mitochondrial ultrastructural abnormalities are *Slc25a1* dosage-dependent. Moreover, as cardiac mitochondria become more elongated and develop more elaborate and organized cristae during cardiac development, our data suggest that SLC25A1 loss impairs mitochondrial structural maturation.

Slc25a1 deletion impairs respiratory chain function in the developing mouse heart

Since our data suggested that *Slc25a1* deletion causes mitochondrial dysfunction, we assessed the impact of *Slc25a1* deletion on mitochondrial respiratory chain function. Respirometry was conducted on E17.5 *Slc25a1*⁺/⁻, *Slc25a1*⁻/⁻, and *Slc25a1*⁺/⁺ hearts. Coupled respiration (supported by glutamate and malate) of *Slc25a1*⁺/⁻ and *Slc25a1*⁻/⁻ hearts was significantly decreased compared to *Slc25a1*⁺/⁺ controls (Fig. 4B). These respiration deficits were also observed with chemical uncoupling by FCCP (carbonyl cyanide-p-trifluoromethoxyphenylhydrazone), indicating that *Slc25a1* deletion also impairs maximal respiratory capacity. Together, these results support impaired oxidative phosphorylation with SLC25A1 loss.

Because defects in mitochondrial cristae ultrastructure have been associated with mitochondrial DNA (mtDNA) depletion[39,40] and the mtDNA encodes essential respiratory chain complex subunits, *Slc25a1* deletion-induced mitochondrial ultrastructural abnormalities (Fig. 4A) could lead to respiration defects by causing mtDNA loss. Thus, we measured mtDNA to nuclear DNA (nDNA) ratios (mtDNA/nDNA) in total DNA isolated from E17.5 *Slc25a1*⁺/⁻, *Slc25a1*⁻/⁻, and *Slc25a1*⁺/⁺ hearts. While

mtDNA/nDNA ratios were not significantly different between *Slc25a1*⁺/⁻ and *Slc25a1*⁺/⁺ hearts, ratios were elevated in *Slc25a1*⁻/⁻ hearts, indicating increased mtDNA content (Fig. 4C). Thus, SLC25A1 deletion-associated respiration defects are not due to mtDNA depletion.

To confirm that SLC25A1 deletion does not alter mitochondrial content in the developing heart, we conducted immunoblotting for TOM20—a ubiquitously expressed subunit of the mitochondrial import machinery—and observed no differences between *Slc25a1*⁺/⁻, *Slc25a1*⁻/⁻, and *Slc25a1*⁺/⁺ control hearts (Supplemental Fig. 6A, B). Collectively, these data suggest that SLC25A1 expression does not impact cardiac mitochondrial content.

We also investigated the impact of *Slc25a1* deletion on respiratory chain complex subunit expression (NDUSFA9 of complex I, SDHA of complex II, UQCRC2 of complex III, COXIV of complex IV, and ATP5A of complex V) by immunoblotting E17.5 total heart lysates (Fig. 4D). *Slc25a1*⁺/⁻ hearts displayed a trend for decreased NDUSFA9, UQCRC2, and ATP5A as well as significantly decreased COXIV compared to controls (Fig. 4E). *Slc25a1*⁻/⁻ hearts displayed significantly decreased expression of all subunits compared to controls (Fig. 4E). Because reduced expression of individual respiratory chain subunits can cause an overall reduction in assembled respiratory chain, we analyzed respiratory chain assembly in mitochondria isolated from E17.5 hearts using blue native polyacrylamide gel electrophoresis (BN-PAGE) and immunodetection for the respiratory chain (Fig. 4F). Cardiac mitochondria from *Slc25a1*⁺/⁻ and *Slc25a1*⁻/⁻ embryos displayed decreased levels of assembled complexes I, III, and V. This *Slc25a1*-dependent decrease in assembled respiratory chain complexes aligns with alterations in metabolic gene expression, subunit expression, mitochondrial ultrastructural abnormalities, and impaired respiration in SLC25 A1-deleted hearts.

Computational modeling predicts metabolic dysregulation and increased glucose dependence with *Slc25a1* deletion

To investigate the overall metabolic consequences of *Slc25a1* deletion in the E17.5 mouse heart, we performed targeted gas chromatography–mass spectrometry (GC-MS) metabolomic profiling on 25 key metabolites, encompassing TCA cycle intermediates, amino acids, and metabolic byproducts that are critical to cardiac energetics (Fig. 5A). Principal component analysis (PCA) as well as unbiased hierarchical clustering of the measured analytes separated samples according to their *Slc25a1* genotype (Fig. 5B, C), with *Slc25a1*⁺/⁻ hearts displaying an intermediate metabolite profile compared to *Slc25a1*⁺/⁺ and *Slc25a1*⁻/⁻ hearts. Citrate was significantly less abundant in *Slc25a1*⁻/⁻ compared to *Slc25a1*⁺/⁺ hearts, while *Slc25a1*⁺/⁻ hearts displayed a trend for reduction (Fig. 5D), indicating that SLC25A1 deletion causes a decrease in cardiac citrate levels. Additionally, glutamate, cystine and lysine abundance increased (Fig. 5D), while threonine, tryptophan, aconitate and pyroglutamate levels were decreased with SLC25A1 deletion. Glutamine and glutamate undergo cyclization to pyroglutamate during the de novo synthesis of gamma-glutamyl cycle of glutathione (l-γ-glutamyl-l-cysteinyl-glycine; GSH). Likewise, cystine is a precursor for GSH synthesis. Hence, the reduced pyroglutamate together with increased glutamate and cystine indicates reduced GSH synthesis with *Slc25a1* deletion.

Because glucose-derived citrate can either be exported from the mitochondria to the cytosol via SLC25A1 or decarboxylated to succinate through the TCA cycle, we compared malate-to-citrate and fumarate-to-malate ratios to assess the incorporation and conversion of citrate-derived carbons within the TCA cycle. With *Slc25a1* deletion, the malate-to-citrate ratio was significantly increased in *Slc25a1*⁻/⁻ hearts compared to controls, while *Slc25a1*⁺/⁻ hearts displayed a trend for an increase (Fig. 5E). However, fumarate-to-malate ratios remained unchanged (Fig. 5F). These data suggest that SLC25A1 deletion reduces citrate incorporation into the TCA cycle thereby limiting oxidative metabolism.

To assess how SLC25A1 deletion impacts metabolic flux in the embryonic heart, we integrated our data using CardioNet[41], a genome-scale metabolic network of cardiac metabolism. To infer flux distributions, we used flux balance analysis and constrained internal metabolite fluxes based
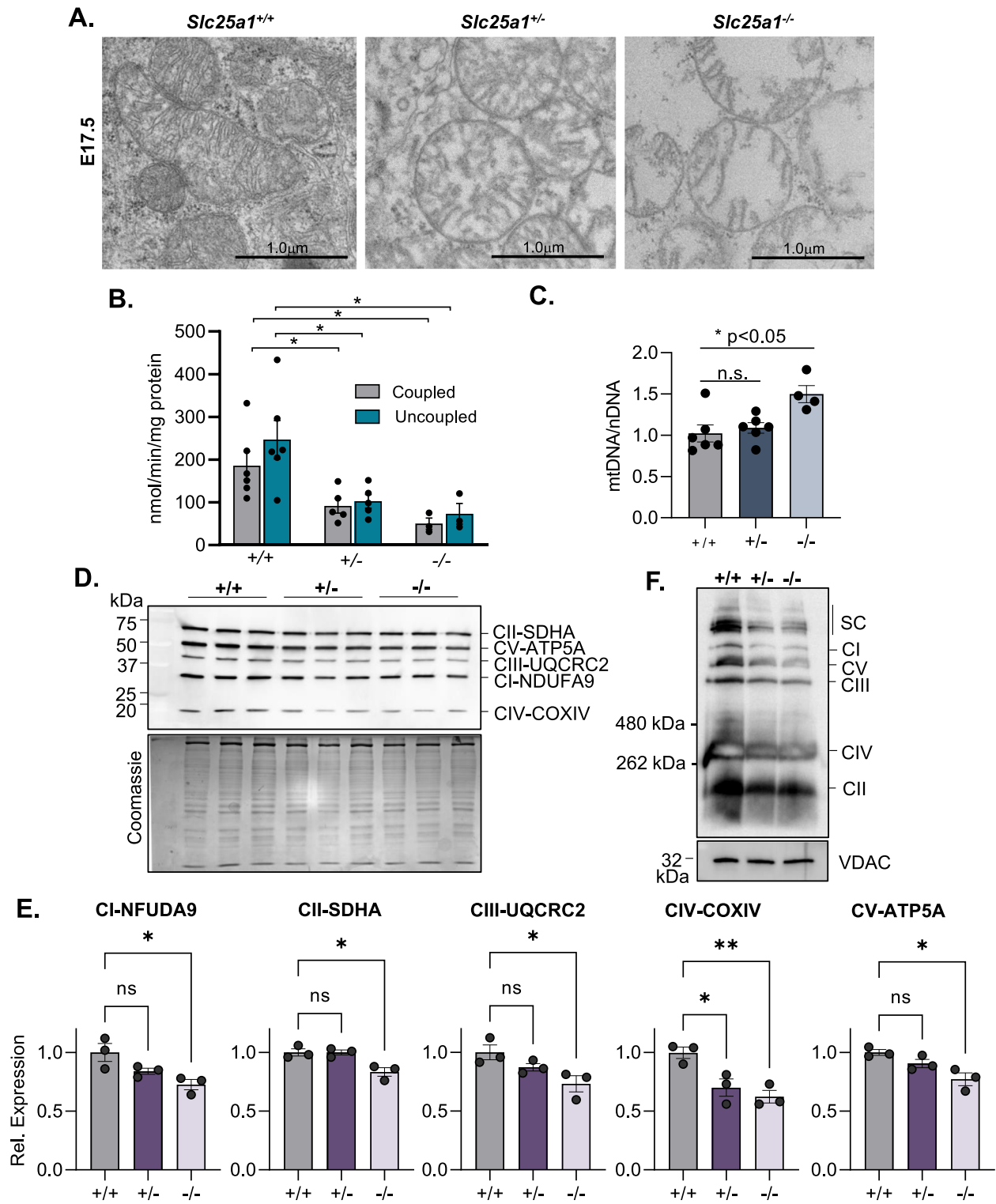
Fig. 4 | *Slc25a1* deletion impairs respiratory chain function in the developing mouse heart. A Representative electron micrographs of cardiac ultrastructure from the indicated genotypes at E17.5 (*n* = 3 *Slc25a1*$^{+/+}$; *n* = 10 *Slc25a1*$^{+/-}$; *n* = 3 *Slc25a1*$^{-/-}$ embryos analyzed). **B** Coupled and uncoupled mitochondrial oxygen consumption rates measured in lightly permeabilized whole E17.5 hearts of the indicated genotypes (*n* = 5 *Slc25a1*$^{+/+}$; *n* = 5 *Slc25a1*$^{+/-}$; *n* = 3 *Slc25a1*$^{-/-}$ hearts analyzed). **C** Quantification of mitochondrial DNA (mtDNA) to nuclear DNA (nDNA) ratios in E17.5 hearts of the genotypes indicated (n = 6 *Slc25a1*$^{+/+}$; *n* = 6 *Slc25a1*$^{+/-}$; *n* = 4 *Slc25a1*$^{-/-}$ embryos analyzed). **D** Western blot of respiratory chain complex subunits (SDHA, ATP5A, UQCRC2, NDUFA9, and COXIV). Coomassie staining of the gel was used as a protein loading control. **E** Densitometry quantification of NDUFA9, SDHA, UQCRC2, COXIV, and ATP5A expression (*n* = 3/group). **F** Respiratory chain complexes in E17.5 heart mitochondria as assessed by BN-PAGE followed by immunoblotting with an OXPHOS antibody cocktail. A western blot of VDAC was used as a protein loading control. Values presented as means ± SEM. One-way ANOVA followed by a post-hoc Dunnett's test. ns denotes not significant; *$P < 0.05$; **$P < 0.005$.
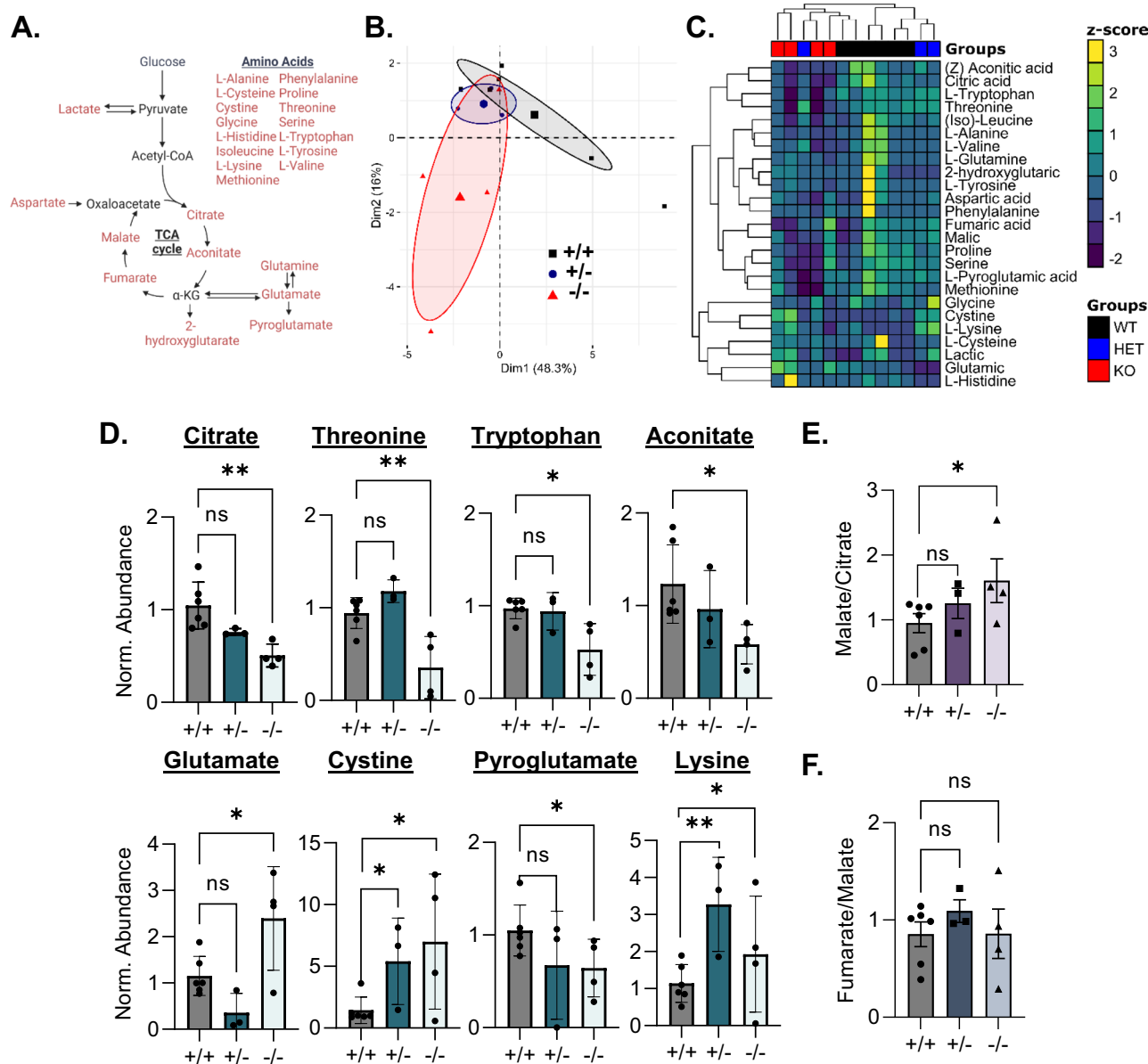
Fig. 5 | Targeted metabolomic profiling reveals amino acid dysregulation and impaired Krebs cycle function with SLC25A1 deletion. A Schematic of the metabolites profiled by GC-MS. **B** Principal component analysis (PCA) and (**C**) unbiased hierarchical clustering of profiled analytes showing clear segregation of $Slc25a1^{+/+}$ ($n = 6$), $Slc25a1^{+/-}$ ($n = 3$), and $Slc25a1^{-/-}$ ($n = 4$) hearts. **D** Normalized abundance of selected metabolites that are significantly altered in HET and KO hearts. Values presented as means ± SEM. One-tailed Student's t test was used for statistical analysis. $P < 0.05$ was considered significant, $*P < 0.05$ and $**P < 0.005$. **E** Malate-to-citrate ratios and (**F**) Fumarate-to-malate ratios in $Slc25a1^{+/+}$, $Slc25a1^{+/-}$ and $Slc25a1^{-/-}$ hearts. Values presented as means ± SEM. One-way ANOVA followed by a post hoc Dunnett's test was used for statistical analysis. $P < 0.05$ was considered significant, ns denotes not significant, $*P < 0.05$.

on our GC-MS-based metabolomics data (Fig. 5), and mitochondrial respiration rates (Fig. 4B). Linear programming was used to calculate solutions that satisfy mass balance and flux constraints. The objective function was defined as a maximization-minimization problem to reflect the requirements of the embryonic heart to maximize ATP provision and biomass synthesis (e.g., protein and membrane lipid synthesis) while minimizing utilization of extracellular substrates and oxygen from the plasma. Flux distributions were analyzed by PCA and among genotype-dependent separation, 80.6% of the total variance was captured in the first two dimensions (Fig. 6A). CardioNet simulations predict increased exogenous glucose utilization with SLC25A1 loss (Fig. 6B, C), which corresponds with increased glycolytic flux and significantly less glucose-derived pyruvate entry into the TCA cycle, which corresponds with reduced TCA cycle flux and ATP provision (Supplemental Fig. 7A, Fig. 6B), as well as

reduced oxidative phosphorylation (Fig. 6D). Correspondingly, we identified reduced glutamine-pyruvate transaminase flux compared to increased glutamic-oxaloacetic transaminase flux (Supplemental Fig. 7B), suggesting that SLC25A1 loss increases glutamine anaplerosis. Ultimately, as embryonic cardiac metabolism matures from dependence on glycolysis to mitochondrial oxidation-derived energy, our simulations suggest that SLC25A1 loss impairs metabolic reprogramming and maturation in the developing heart.

Slc25a1 deletion reduces histone acetylation in developing mouse hearts

Our combined transcriptomics, biochemical, and metabolomics analyses revealed defects in mitochondrial oxidative metabolism with *Slc25a1* deletion. We next assessed potential mechanisms that control *Slc25a1*
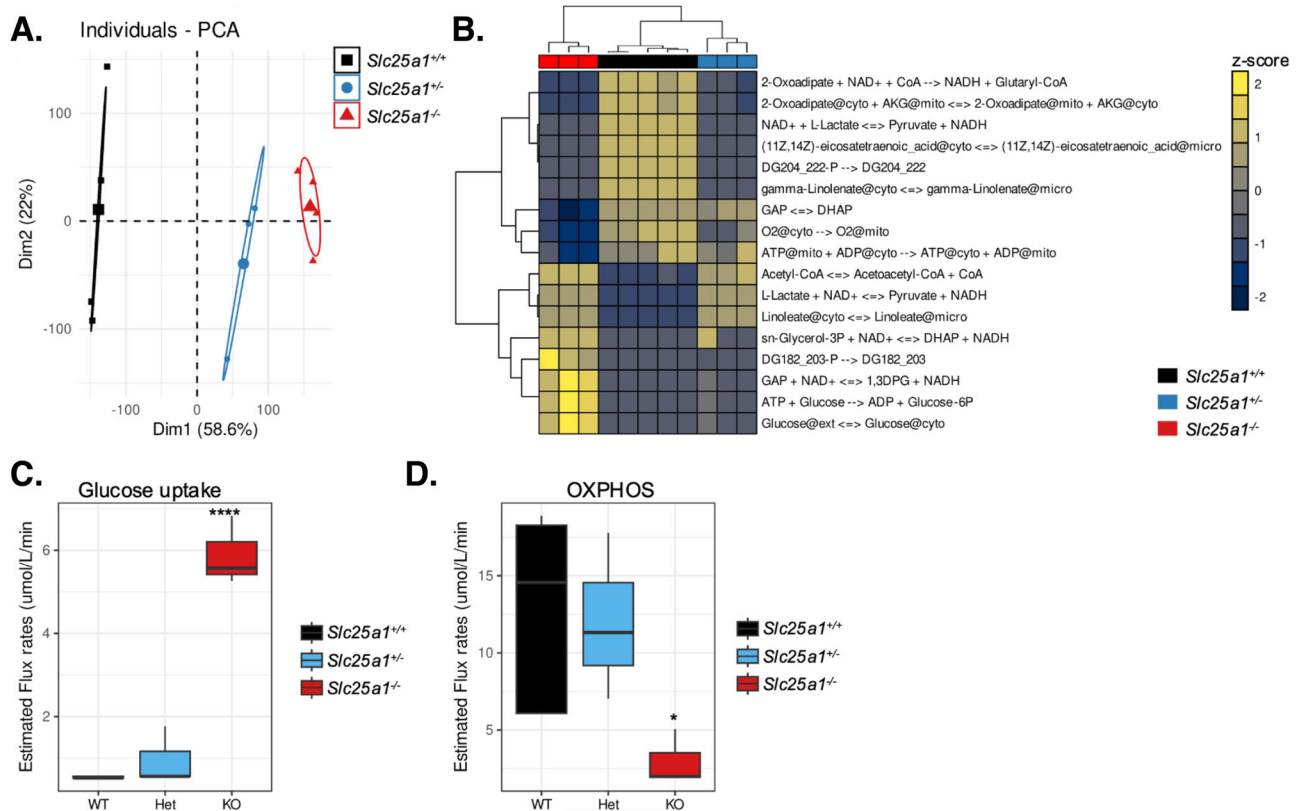
Fig. 6 | In silico modeling reveals glucose dependency and impaired oxidative phosphorylation with SLC25A1 loss. A PCA of the CardioNet simulation revealed a clear clustering of *Slc25a1*^{+/+}, *Slc25a1*^{+/-}, and *Slc25a1*^{-/-} hearts by *Slc25a1* genotype. **B** Unsupervised hierarchical clustering of significantly altered flux distributions. Two-way ANOVA with post hoc Tukey's test followed by multiple comparison analysis (FDR < 1% after Benjamini, Krieger and Yekuteli). **C** Predicted flux rates for glucose uptake, and **D** oxidative phosphorylation in response to SLC25A1 deletion. Box plot parameters are defined by the minimum value, the first quartile, the median, the third quartile, and the maximum value. *$P < 0.05$; ****$P < 0.00005$.

deletion-associated metabolic dysregulation. SLC25A1 is the main mitochondrial transporter for citrate export[10,11]. In the cytosol, citrate is converted to acetyl-CoA, a substrate for epigenetic modifications like histone acetylation[17,18]. As acetyl-CoA abundance modulates histone acetylation, SLC25A1 could connect mitochondrial metabolism to epigenetic gene regulation via modulating citrate. To determine whether the decreased citrate levels in *Slc25a1*^{+/-} and *Slc25a1*^{-/-} hearts (Fig. 5D), alters histone acetylation, we assessed acetylation of histone H3 at lysine 9 (H3K9), which is often enriched at promoters of actively transcribed genes[42], by immunoblots of total extracts from E17.5 hearts (Fig. 7A). The ratio of acetylated H3K9 (H3K9ac) to total histone H3 was reduced in *Slc25a1*^{+/-} and *Slc25a1*^{-/-} hearts compared to *Slc25a1*^{+/+} controls (Fig. 7B), suggesting that SLC25A1 regulates histone acetylation in the developing heart.

We next postulated that SLC25A1-related histone acetylation changes could affect gene expression. Given technical challenges in profiling gene expression in large numbers of embryonic hearts, we chose a candidate gene approach as a proof of concept. Because SLC25A1 deletion caused a striking decrease in respiration, we focused on mitochondrial metabolism genes that were both dysregulated in the NanoString panel (*Ndufa1*, *Ndufb4*, *Ndufs8*, Ndufb2, *Ndufb8*, *Uqcrq*, *Cox4i1*, *Cox5b*, and *Pdha*) and had H3K9ac promoter enrichment assessed by analyses of publicly available H3K9ac chromatin immunoprecipitation-sequencing (ChIP-seq) datasets[42,43] (Supplemental Figure 8A). We additionally prioritized *Pparg* for analysis because it is a transcription factor that regulates metabolic gene expression[44] that is significantly dysregulated in our transcriptomics analysis, has H3K9ac promoter enrichment (Supplemental Fig. 8A), and cardiomyocyte-specific deletion phenocopies the VSDs[45] observed in *Slc25a1* deleted embryos. Moreover, analysis of the SLC25A1 deletion-dysregulated metabolism genes identified *Pparg* as a top potential transcriptional regulator

(Supplemental Fig. 8B). Thus, to test the possibility that SLC25A1 impacts the expression of these candidate genes by regulating H3K9ac promoter enrichment, we performed H3K9ac ChIP followed by quantitative PCR (qPCR) to assess H3K9ac promoter abundance in E17.5 hearts. Our results revealed significantly reduced H3K9ac at the promoters of *Ndufa1*, *Ndufb4*, *Ndufs8*, *Ndufb2*, *Ndufb8*, *Uqcrq*, *Cox5b*, *Pdha1*, and *Pparg* in *Slc25a1*^{+/-} and *Slc25a1*^{-/-} hearts compared to *Slc25a1*^{+/+} controls, and a trend for decreased H3K9ac at the *Cox4i1* promoter (Fig. 7C). These results support an epigenetic role for SLC25A1, in which SLC25A1 alters histone acetylation to regulate gene expression in the developing heart.

Discussion

Previous investigations have associated SLC25A1 with several diseases[24,26,30-32,36]. Our results here provide new evidence that SLC25A1 also contributes to metabolic reprogramming during cardiac development. Our mouse model results show that systemic loss of SLC25A1 led to stunted embryonic growth, perinatal lethality, and developmental abnormalities including cardiac structural defects. Moreover, SLC25A1 loss resulted in mitochondrial dysfunction and perturbations in metabolic gene expression, and derangements in cardiac mitochondrial ultrastructure and function that collectively point to a role for SLC25A1 in metabolic reprogramming during mouse heart development. Importantly, *Slc25a1* haploinsufficiency was sufficient to produce cardiac developmental defects, which may underscore the clinical relevance of our findings.

Our initial efforts to identify the mechanisms by which *Slc25a1* deletion reduces respiratory chain function in the embryonic mouse heart led us to examine the relationship between SLC25A1 and the mitochondrial ribosome, as SLC25A1 regulates mitochondrial ribosome subunit expression in vitro[21]. Our analyses of E17.5 hearts did not reveal
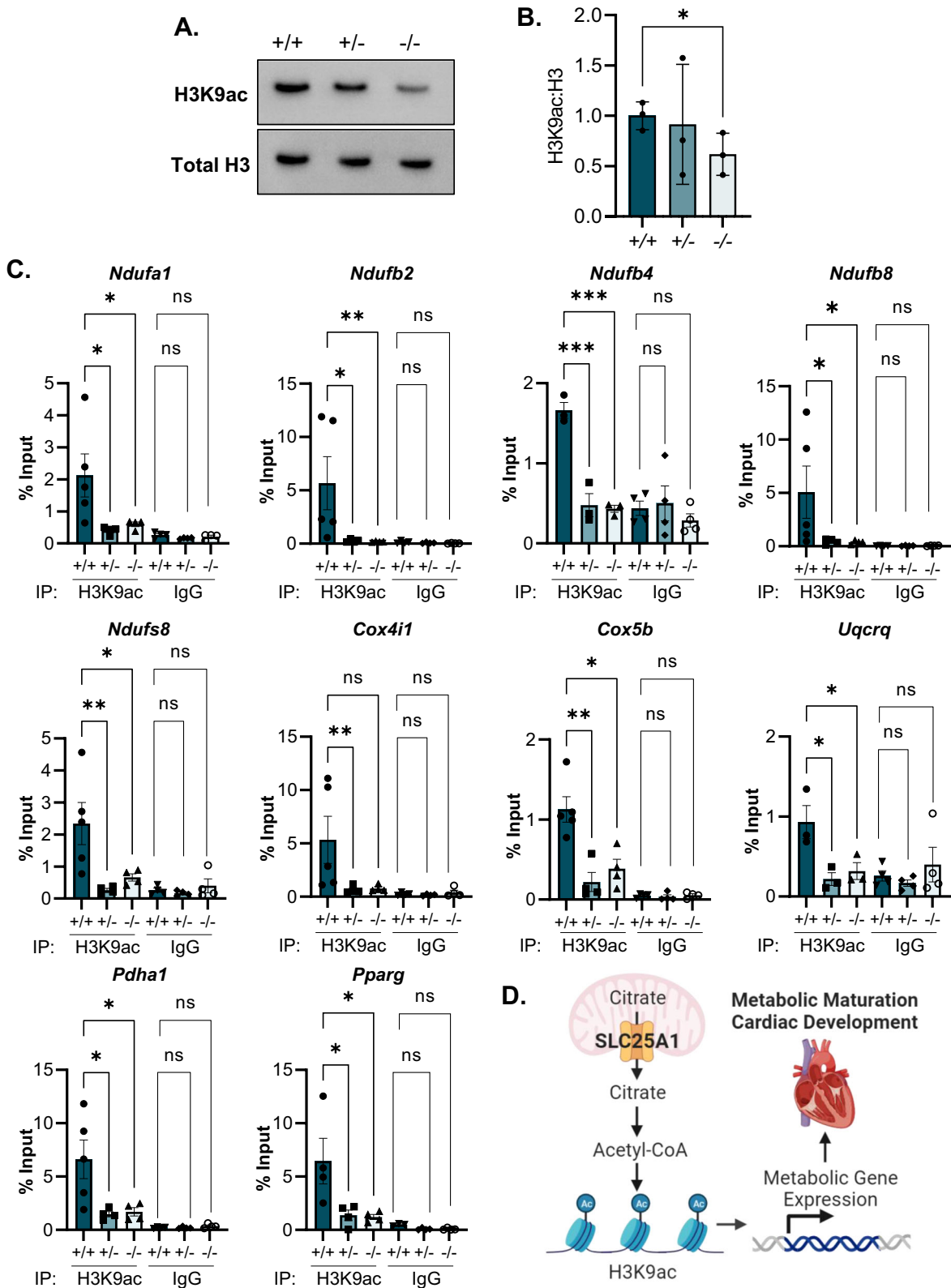
any alterations in protein expression of key mitochondrial ribosome subunits with SLC25A1 loss, indicating that *Slc25a1* deletion-induced mitochondrial dysfunction is not due to impaired mitochondrial translation. Because the mitochondrial proteome and function can differ between different tissues and cell types[46,47], our data point to possible cell type- and tissue-specific effects of SLC25A1.

Our studies of metabolic gene expression revealed intriguing consequences of SLC25A1 deletion. First, hierarchical analysis of differentially expressed genes revealed a *Slc25a1* dosage-dependent dysregulation of metabolic genes that parallels the dosage-dependent frequency/degree of severity of cardiac malformations observed in vivo. Moreover, while gene ontology analysis revealed organic acid transport as a significant pathway

Fig. 7 | *Slc25a1* deletion reduces histone acetylation at promoter of metabolism-related genes in developing mouse hearts. A Representative western blot of histone H3 acetylated at K9 (H3K9ac) and total histone H3 in total heart protein from E17.5 embryos of the indicated genotypes. **B** Densitometry quantification of H3K9ac to H3 levels in E17.5 hearts (*n* = 3/group). One-way ANOVA followed by post hoc Dunnett's test was used for statistical analysis. *$P < 0.05$. **C** H3K9ac ChIP qPCR of H3K9ac enrichment at the promoters of *Ndufa1*, *Ndufb2*, *Ndufb4*, *Ndufb8*, *Ndufs8*, *Cox4i1*, *Cox5b*, *Uqcrq*, *Pdha1* and *Pparg* in E17.5 hearts (*n* = 4-5/group). ChIP with anti-rabbit IgG was used as a negative control. Data were normalized using input

DNA. Values presented as means ± SE. One-way ANOVA followed by post hoc Dunnett's test was used for statistical analysis. ns denotes not significant; *$P < 0.05$, **$P < 0.005$, and ***$P < 0.0005$. **D** Proposed model of SLC25A1-mediated citrate export and its role in regulation of metabolic gene expression in the developing heart. Citrate in the mitochondria is generated from acetyl-CoA and oxaloacetate in the TCA cycle. SLC25A1 mediates mitochondrial citrate export. Citrate in the cytosol is converted to acetyl-CoA, which is used for histone acetylation (H3K9ac) and impacts gene expression necessary for proper heart development. Diagram created using BioRender.

impacted by SLC25A1 deletion—anticipated given that SLC25A1 itself is an organic acid transporter—AMPK signaling and positive regulation of cell death unexpectedly also emerged as key pathways. AMPK signaling is a critical metabolic pathway that mediates a coordinated response to energy dysregulation[48], and the identification of this pathway reinforces the dysregulation of pathways like OXPHOS and glycolysis that we identified by GSEA, as well as mitochondrial dysfunction we observed by respirometry. Notably, increased cell death during cardiac morphogenesis can perturb cardiac structural maturation[49–51], suggesting that SLC25A1 deletion-associated upregulation of cell death may contribute to observed cardiac malformations.

Integrating our mitochondrial functional studies, transcriptomics, metabolomics, and in silico studies to understand the metabolic ramifications of SLC25A1 deletion confirmed dosage dependency of metabolic dysregulation and highlighted the critical role of SLC25A1 in metabolic reprogramming in the developing mouse heart. We found that SLC25A1 loss causes dysregulation of cardiac metabolism by increasing glucose utilization and glutamine anaplerosis while impairing TCA cycle flux and oxidative metabolism. The immature developing heart is mainly fueled by glycolytic ATP, while the maturing heart incorporates a wide-range of substrates including fatty acids, ketone bodies and amino acids. Our multi-omics analysis indicates that SLC25A1 loss leads to an 'immature' metabolic profile, whereby SLC25A1 deleted hearts remain reliant on glucose with impaired oxidative metabolism.

How can the focal loss of a mitochondrial transporter result in such widespread changes to the metabolic landscape of the developing heart? SLC25A1 transports mitochondria-produced citrate to the cytosol[14,15]. As part of the TCA cycle, mitochondrial citrate is formed from condensation of acetyl-CoA and oxaloacetate and is further oxidized to enable oxidative energy production[52]. In the cytosol, citrate can be converted back into acetyl-CoA by ATP-citrate lyase[53]. Acetyl-CoA is an essential substrate for protein post-translational acetylation and epigenetic regulation of gene expression via histone acetylation and cellular acetyl-CoA levels modulate histone acetylation status[18,53]. As acetyl-CoA cannot cross the inner membrane, SLC25A1 may link mitochondrial metabolism to epigenetic regulation of gene expression by modulating acetyl-CoA compartmentalization via citrate.

Our proof-of-concept ChIP of metabolism-related genes suggest a critical role for SLC25A1 in regulating gene expression in the developing heart through H3K9 acetylation (Fig. 7D). We found that SLC25A1 loss results in decreased total H3K9ac in the developing heart, leading to reduced H3K9ac at the promoters of mitochondrial metabolism-associated genes, which aligns with our observed reduction in metabolic gene expression and mitochondrial respiration of SLC25A1 deleted hearts. As embryos with cardiomyocyte-specific deletion of PPARγ phenocopy the VSDs we observed in mouse embryos with systemic *Slc25a1* deletion[45], our finding of reduced H3K9ac at the PPARγ promoter further support a link between SLC25A1 and PPARγ in the developing heart. Collectively, our findings indicate that SLC25A1 is a mitochondrial regulator of genetic reprogramming required for oxidative metabolism in the maturing heart.

Our discovery that *Slc25a1* KO embryos display cardiac malformations and mitochondrial dysfunction is notable but could be expected. However, one striking finding of our study is that *Slc25a1* haploinsufficiency in mice also produces cardiac malformations and mitochondrial dysfunction, generating a clinical connection to CHD. In humans, *SLC25A1* is located on chromosome 22q11.2 within the critical deletion region associated with 22q11.2DS[22]. Cardiac presentations of 22q11.DS commonly include

conotruncal defects like VSDs, tetralogy of Fallot[23], and left ventricular noncompaction[54,55]. Cardiac defects associated with 22q11.2DS have largely been ascribed to TBX1, a transcription factor located in the critical deletion region that plays important roles in cardiovascular development[56]. Yet, 22q11.2DS is a syndrome of haploinsufficiency and *Tbx1* haploinsufficiency does not reproduce the full spectrum of cardiac defects associated with 22q11.2DS; thus, additional factors must contribute to its cardiac phenotypes. Because partial loss of *Slc25a1* in mice is sufficient to produce CHD observed in 22q11.2DS, our data position *SLC25A1* as a novel 22q11.2 gene that contributes to the cardiac presentation of 22q11.2DS.

Additionally, *SLC25A1* variants underlie two rare autosomal recessive neurometabolic/neuromuscular disorders, DL-2HGA and CMS23[30–32]. While cardiac disease is not part of the OMIM characterization of these disorders, there have been hints that *SLC25A1* variants may also impact the heart. VSDs, atrial septal defects, patent ductus arteriosus, bicommissural aortic valve, and patent foramen ovale were reported in isolated cases of DL-2HGA due to *SLC25A1* variants[57–59]. Our analyses of the PCGC dataset demonstrates a trend towards an association of ultrarare *SLC25A1* variants (a limitation being one-stop only stop-gain variant alongside missense variants of uncertain significance identified) with pediatric CHD, and may suffer from type II error. While our *SLC25A1* variant burden testing did not reach statistical significance, it is important to note that our studies of the *Slc25a1* KO mouse model support neonatal lethality of *Slc25a1*^{+/-} pups before P7. As such, predicted damaging *SLC25A1* variants may be underrepresented in the PCGC cohort due to lethality of undiagnosed neonates. Further, the CHDs associated with ultrarare damaging *SLC25A1* variants (VSDs, tetralogy of Fallot, and conotruncal defects) align with the malformations associated with 22q11.2DS. We also previously discovered that *SLC25A1* affects neurodevelopment in 22q11.2DS[24], and some DL-2HGA patients exhibit microcephaly[57], a feature we also observed in *Slc25a1*^{-/-} mouse embryos. Together, our work suggests that *SLC25A1* is a nuclear DNA-encoded mitochondrial gene that can connect the neurological and cardiac pathologies of 22q11.2DS and DL-2HGA.

We have uncovered a novel pathway of metabolic regulation in which SLC25A1 regulates gene expression in the developing heart. We demonstrated that *Slc25a1* is a dosage-dependent regulator of ventricular morphogenesis in the developing mouse embryo. Critically, our work in *Slc25a1* KO mice has clinical relevance, as we identified a strong trend for pathogenic variants of human *SLC25A1* to associate with CHD. Collectively, our work positions SLC25A1 as a mitochondrial transporter that mediates epigenetic regulation of gene expression in the developing heart and highlights a role for SLC25A1 in metabolic maturation in heart development. As SLC25A1-dependent regulation of gene expression may extend beyond metabolism, our work opens the door to a potential broader role for SLC25A1 in mitochondrial control of developmental programs. Finally, as *SLC25A1* is a 22q11.2 gene, and our studies point to a role for *SLC25A1* as novel CHD risk factor, this study may be an important first step in defining SLC25A1 as a connection between cardiac and neurodevelopmental pathologies in 22q11.2DS.

Methods
Animals
Slc25a1tm1a(EUCOMM)Wtsi KO-first mutant mice (*Slc25a1*^{+/-}) were obtained from the Mutant Mouse Resource and Research Center at the University of California, Davis and maintained on a C57BL6/J background. Timed matings were established using 2–3-month-old *Slc25a1*^{+/-} male and

female mice, with the morning of an observed copulation plug established as E0.5. Experiments were conducted on male and female embryos collected at E10.5, E12.5, E14.5, E17.5, and E18.5. Genotyping of Slc25a1^{+/-} mice as well as embryos from Slc25a1^{+/-} intercrosses was conducted on genomic DNA isolated from embryonic yolk sacs or tail biopsies. All animal experiments were carried out with experimental protocols reviewed and approved by Emory University's Institutional Animal Care and Use Committee in compliance with ethical regulations for animal use.

Histology and immunostaining
Hearts were fixed in 10% formalin and embedded in paraffin. Paraffin-embedded tissues were sectioned (6 µm), deparaffinized, rehydrated, stained with hematoxylin and eosin (H&E), and imaged using a Nano-zoomer 2.0-HT whole-slide scanner (Hamamatsu). Myocardial trabecular and compact layer thicknesses were measured on H&E-stained sections using QuPath image analysis software[60].

For immunofluorescence, paraffin-embedded sections were deparaffinized and rehydrated, and antigen retrieval was performed with citrate buffer (pH 6.0). The following primary antibodies were used: anti-myosin heavy chain (Developmental Studies Hybridoma Bank, MF20, 1:20), anti-SLC25A1 (Proteintech, 15235-1-AP, 1:100), and anti-ATP5A (Abcam, ab14748, 1:200). Secondary antibodies used were: donkey anti-mouse 488, and donkey anti-rabbit 594 (1:200, Cell Signaling Technologies). Slides were mounted with ProLong Gold Antifade Mountant with DAPI (Thermo Fisher Scientific) to counterstain nuclei or ProLong Gold Antifade Mountant (Thermo Fisher Scientific). Fluorescence imaging was conducted using a Keyence BZ-X810 system or a Leica Stellaris confocal microscope.

Whole exome sequencing and burden testing
Genomic analysis using the Pediatric Cardiac Genomic Consortium (PCGC) whole exome cohort followed published protocols[61–63]. Briefly, whole-exome DNA from blood or salivary samples was captured using the Nimblegen v.2 exome capture reagent (Roche) or Nimblegen SeqxCap EZ MedExome Target Enrichment Kit (Roche), followed by Illumina DNA sequencing as previously described[61–63]. The resulting sequencing data were processed at Yale University School of Medicine, and reads were mapped to the hg19 reference genome. Mapped reads were further processed using the GATK Best Practices workflows[64], as previously described[61]. Single nucleotide variants and small indels were called with GATK HaplotypeCaller[65]. Further data filtering was performed using plink[66], including removing individuals with low call rates, outlying heterozygosity rates, outlying relatedness rates, and sex discrepancy. A total of 3740 probands passed individual filtering, and there were a remaining 3401 complete trios. A case-control cohort was generated for all complete trios using pseudo-sibling controls. With this method, a proband's genotypes are taken as the case, and a pseudo-control sample is created with all untransmitted alleles between the parents and the proband using plink[67]. Variants were filtered on call rate, Hardy-Weinberg equilibrium, and a high number of Mendel errors (≥3). Variants within SLC25A1 were extracted using the longest known canonical hg19 SLC25A1 variant bed file downloaded from UCSC TableBrowser on 4/5/23[68]. The remaining variants were annotated using wANNOVAR[69]. Loss of function (frameshift, splice site, start lost, stop gained, and stop loss) and missense variants with combined annotation-dependent depletion score >20[70] and minor allele frequency <0.001 in all gnomAD[71] populations were kept for burden analysis. An additional "ultrarare" variant set was created by keeping SLC25A1 variants that do not occur in the gnomAD exome database (v2.1.1, as of 4/12/23). Burden testing using the pseudo-sibling-controlled cohort was performed using kernel based adaptive cluster methods using WISARD[72]. The Bonferroni correction for multiple testing was used, establishing an alpha level of 0.0167.

Echocardiography
Mice were anesthetized with isoflurane (1.5%), and body temperature was maintained at 37 °C. Echocardiography measurements were performed using a Vevo 2100 Imaging System (VisualSonics) equipped with a MS-400

transducer. M-mode and B-mode measurements were taken of the para-sternal short- and long-axis views. Systolic and diastolic ventricular chamber dimensions as well as left and right ventricular wall thicknesses were assessed. Ejection fraction, fractional shortening, and stroke volume were calculated using VevoLab software.

Metabolic gene expression profiling
Transcriptomic profiling of expression of 768 metabolism-related genes was conducted using the NanoString nCounter Mouse Metabolic Pathways Panel. Briefly, total RNA was isolated from E17.5 hearts (n = 4/genotype) using a RNeasy Micro Kit (Qiagen). NanoString processing was completed by the Emory Integrated Genomics Core. RNA quality was assessed with the NanoString protocol. mRNA counts were normalized by expression of the housekeeping gene Tbp. Data were analyzed using Qlucore Omics Explorer Version 3.7(24) or GSEA v4.3.2. Differentially expressed mRNAs from QLUCORE were analyzed with the Metascape engine to determine ontology enrichment as well as representation of transcription factors using TRRUST. GSEA analysis was used to query the REACTOME database[73].

Transmission electron microscopy
Mouse heart samples were collected from E17.5 embryos and fixed in 2.5% glutaraldehyde in 0.1 M cacodylate buffer (pH 7.4). Hearts were subsequently postfixed in 1% osmium tetroxide and embedded in epoxy resin. Ultrathin sections (80–90 nm) were cut with a Leica EM CU6 microtome and counterstained with uranyl acetate and lead citrate. Sections were imaged on a JEOL JEM-1400 transmission electron microscope (Tokyo, Japan) equipped with a Gatan US1000 CCD camera (Pleasanton, CA). Mitochondrial morphology was quantified as previously described in ref. 74 using ImageJ software (NIH).

Electrophoresis and immunoblotting
For western blots, total protein extracts were prepared from embryonic hearts solubilized in radioimmunoprecipitation assay buffer supplemented with combined protease/phosphatase inhibitor cocktail (Thermo Fisher Scientific). Proteins were resolved on 10% SDS-PAGE gels (TGX stain free gels, BioRad), transferred to PVDF membranes, immunodetected with antibodies, and imaged using a ChemiDoc XRS+ system (BioRad). Primary antibodies used were: anti-SLC25A1 (Proteintech, 15235-1-AP, 1:1000), anti-TOM20 (Proteintech, 11802-1-AP, 1:1000), OXPHOS Blue Native WB Antibody Cocktail (contains antibodies against SDHA ATP5A, UQCRC2, NDUFA9, and COXIV; Abcam, ab110412, 1:500), anti-H3K9ac (Cell Signaling Technologies, 9649, 1:1000), anti-H3 (Cell Signaling Technologies, 4499, 1:1000), anti-VDAC (Proteintech, 55259-1-AP, 1:1000) and anti-GAPDH (Fitzgerald, 10 R-G109A, 1:10,000). Secondary antibodies used were alkaline phosphatase-linked goat anti-rabbit IgG (Cell Signaling Technologies, 7054), alkaline phosphatase-linked goat anti-mouse IgG (Cell Signaling Technologies, 7056), horseradish peroxidase-linked goat anti-mouse IgG (Cell Signaling Technologies, 7076), and horseradish peroxidase-linked goat anti-rabbit IgG (Cell Signaling Technologies, 7074). Blots were imaged using a ChemiDoc XRS+ System (BioRad) and quantified using Image Lab software (BioRad).

Blue native polyacrylamide gel electrophoresis
BN-PAGE and immunoblotting for mitochondrial respiratory complexes were performed using pooled E17.5 hearts (n = 6/genotype), as previously described[75]. 50ug mitochondrial extracts from the pooled hearts were solubilized with digitonin (Sigma Aldrich, 4 g/g digitonin/protein ratio) and separated on a NativePAGE 3–12% Bis-Tris polyacrylamide gradient gel (Invitrogen). Proteins were transferred to a PDVF membrane and immunoblotting for respiratory complexes was conducted with the Total OXPHOS Blue Native WB Antibody Cocktail (Abcam, ab110412, 1:250) at 4 °C overnight. The membrane was washed in TBST and incubated in horseradish peroxidase-linked anti-mouse IgG (Cell

Signaling Technologies, 7076, 1:5000). The blot was developed using Clarity Max Western ECL Substrate (BioRad) and imaged using the BioRad Chemidoc XRS+ System.

Mitochondrial oxygen consumption

Mitochondrial oxygen consumption was conducted on embryonic hearts as previously described[76]. Briefly, hearts were harvested from E17.5 embryos. Hearts were gently homogenized on ice in isolation buffer (225 mM mannitol, 10 mM sucrose, 0.5 mM EGTA, 10 mM HEPES, pH 7.4). The heart homogenate was diluted in respiration buffer (70 mM mannitol, 25 mM sucrose, 20 mM HEPES, 120 mM KCl, 5 mM KH_2PO_4, 3 mM $MgCl_2$, pH 7.4) containing 5 mM glutamate and 3 mM malate. Oxygen consumption was measured using an Oxytherm System (Hansatech). Basal ADP-stimulated respiration was initiated with the addition of 1 mM ADP, uncoupled respiration was induced with the addition of 0.3 μM FCCP, and nonmitochondrial oxygen consumption was assessed with the addition of KCN. Basal and maximal uncoupled mitochondrial oxygen consumption rates were obtained by subtracting KCN-nonmitochondrial respiration, followed by normalization to protein concentration measured by Bradford assay (BioRad).

mtDNA copy number analysis

Total DNA was prepared from snap-frozen embryonic heart tissue using a DNAeasy Kit (Qiagen). Four E17.5 hearts per genotype were pooled for each replicate ($n = 4$ replicates/genotype). Quantification of relative mtDNA copy number was conducted by measuring mtDNA/nDNA ratio using qPCR. Primers for mouse mtDNA (forward, CTA-GAAACCC-CGAAACCAAA; reverse, CCAGCTATCACCAAGCTCGT) and the β-2-microglobulin nuclear DNA (forward, 5' ATGGGAAGCCGAACA-TACTG 3'; reverse, 5' CAGTCTCAGTGGGGGGTGAAT 3') were used as previously described in ref. 77. qPCR was performed using LightCycler 480 SYBR Green I Master (Roche) on an Applied Biosystems Quant-Studio 6 Flex Real-Time PCR system. Relative mtDNA copy number was calculated using the ΔΔC(t) method.

Gas chromatography and mass spectrometry (GC/MS)-based targeted metabolomics

Metabolites were isolated as described previously[78]. Briefly, frozen heart tissue sample were homogenized in 0.4 mL −80 °C cold MS-grade methanol, acetonitrile, water at a volume ratio of 40:40:20 (v/v/v/). Further disruption of tissue sample was achieved by freeze-thawing sample three-times. Extracts were centrifuged at 13,000 rpm for 5 min at 4 °C. The supernatant was transferred to clean glass tubes and D27-myristic acid (0.15 μg/μL, Cat No 366889, Sigma- Aldrich; St Louis, MO) was added as internal run standard. Vials were covered with a breathable membrane and metabolites were evaporated to dryness under vacuum. Dried samples were stored at −80 °C for further GC-MS analysis. For derivatization of polar metabolites frozen and dried metabolites from cell extractions were dissolved in 20 μL of Methoxamine (MOX) Reagent (2% solution of methoxyamine-hydrogen chloride in pyridine; Cat. No. 89803 and 270970; Sigma- Aldrich; St Louis, MO) and incubated at 30 °C for 90 min. Subsequently, 90 μL of N-tert-Butyldimethylsilyl-N-methyltrifluoroacetamide with 1% tert-Butyldimethyl-chlorosilane (TBDMS; Cat. No. 375934, Sigma- Aldrich; St Louis, MO.) was added and samples were incubated under shaking at 37 °C for 30 min. GC-MS analysis was conducted using an Agilent 8890 GC coupled with a 5977-mass selective detector. Metabolites were separated on an Agilent HP-5MS Ultra Inert capillary column (Cat.No. 19091S-433UI). For each sample, 1 μL was injected at 250 °C using helium gas as a carrier with a flow rate of 1.1064 mL/min. For the measurement of polar metabolites, the GC oven temperature was kept at 60 °C and increased to 325 °C at a rate of 10 °C/min (10 min hold) followed by a postrun temperature at 325 °C for 1 min. The total run time was 37 min. The MS source and quadrupole were kept at 230 °C and 150 °C, respectively, and the detector was run in scanning mode, recording ion abundance within 50 to 650 m/z.

Mathematical modeling of the myocardial metabolic adaptations in the embryonal heart

In silico simulations were performed using the metabolic network of the cardiomyocyte CardioNet[41,78,79]. Mathematical modeling can accurately predict the dynamics of cardiac metabolism in response to stress, and CardioNet can identify metabolic profiles and flux distributions. Flux balance analysis (FBA) allows to estimate flux rates by integrating experimental constraints on metabolites or proteins within a defined biochemical network. We specified flux constraints for extracellular metabolites reflecting the circulating metabolite composition in fetal plasma. Intracellular metabolites were constrained using experimentally determined metabolite abundance (GC-MS). Based on these constraints we first determined flux distributions (v_m) under $Slc25a1^{+/+}$ (control) conditions. We then calculated fold-changes (FC) for experimentally measured metabolite concentrations between control and experimental groups ($Slc25a1^{++}$ and $Slc25a1^{-/-}$) and used these fold-changes to further constrain fluxes (v_m) for the synthesis and/or degradation of intracellular metabolites. We included fold-changes (FC) based on the assumption that changes in metabolite concentrations under experimental conditions are accompanied by a proportional increase or decrease in the respective flux for the metabolite pool. By using metabolite level changes (fold changes) to estimate flux rate changes (v_{FC}), we imply that the altered steady-state concentrations of metabolites are reflected in the newly evolved flux state and potentially limit metabolic functions.

To reflect the unique growth requirements in the fetal heart, we defined a biomass function including the synthesis of structural proteins, membrane lipids and ATPase activity[41]. Linear problems were defined for experimental group to identify steady-state flux distributions that fulfill the applied constraints (e.g., substrate uptake and release rates), as well as changes in the metabolite pools. Regular FBA seeks to minimize the sum of all internal fluxes to fulfill applied constraints and the steady conditions[41]. However, in the context of a growing heart this condition may not yield correct flux estimations, because the maximization of biomass is not reflected in a regular minimization optimization problem. Instead, we defined the objective as a maximin problem, which maximizes the minimum objective (e.g., flux) for all a given set of internal constraints[41]

$$\text{maximize } z$$
$$\text{subject to}$$

$$S \cdot v = 0,$$

$$v_i^{(-)} \leq v_i \leq v_i^{(+)},$$

$$L_j^{(-)} \leq v_j \leq L_j^{(+)} \left(j = j_1, j_2, \ldots \right),$$

$$v_m \leq FC_m \cdot v_m^0 \left(m = m_1, m_2, \ldots \right),$$

$$BIOMASS = v_{ATPase} + v_m + v_{contractile\ protein} + v_{lipids},$$

$$z \leq v_m,$$

$$z \leq v_{ATPase},$$

$$z \leq v_{contractile\ proteins},$$

$$z \leq v_{lipids}$$

where v_i denotes the flux rate change through reaction i, v_j denotes the measured uptake or secretion rate through reaction j, S is the stoichiometric

matrix, $v_i^{(-)}$ and $v_i^{(\mp)}$ are flux constraints, and z that is an upper bound for each of the individual variables within the biomass function. Linear problems were implemented in perl and solved using the GUROBI LP solver[80]. The resulting fluxes were compared between groups using a two-way ANOVA followed by multiple comparisons analysis. Adjusted q-values were computed using the Bonferroni, Krieger and Yekuteli two-step method.

ChIP-qPCR and analyses of ChIP-seq data

ChIP experiments were conducted using the Magna ChIP HiSens Chromatin Immunoprecipitation Kit (EMD Millipore) with modifications. Briefly, E17.5 hearts were collected and pulverized with a mortar and pestle in liquid nitrogen. DNA–protein interactions were preserved with crosslinking buffer at continuous rotation for 20 min. The crosslinking reaction was stopped with addition of 2.5 M glycine. Following centrifugation (2000 g for 15 min) and washing with cold 1X PBS, samples were centrifuged again (2500 g for 10 min). Nuclei isolation buffer and sonication/ChIP/wash buffer were added to each sample for cell lysis and release of crosslinked protein–DNA. Samples were sonicated on ice with Misonix XL-2000 output 3 for 50 cycles of 15 s with a 45 s refractory period. ChIP was performed according to the manufacturer's instructions. Antibodies used were: anti-H3K9ac (Sigma Aldrich, 17-658), and normal rabbit IgG (Sigma Aldrich, 12-370). Immunoprecipitated and input DNA was subjected to qPCR on a CFX96 Touch Real-Time PCR Detection System (BioRad) using SsoAdvanced Universal SYBR Green Supermix (Bio Rad 172-5270). The following primer sets were used to amplify targeted promoter regions: *Pparg* forward, 5' CTGCGTAACTGACAGCCTAACC 3' reverse, 5' CTTGTGTGACTTCTCCTCAGCC 3'; *Ndufa1* forward, 5' CCCCGTTGGTGAATTTGTGG 3' reverse, 5' GCGGAGATGTGGTTCGAGAT 3'; *Pdha1* forward, 5' AGAACTAGGCCCTCAGACGA 3', reverse, 5'CATGAGGAAGATGCTTGC CG 3'; *Ndufs8* forward, 5' AACCTGCAGAGTGACCTTGG 3', reverse,5' TTGAACCGCATC TGGGCC 3'; *Cox4i1* forward, 5' TCTGAAACGGACGGGCTTG 3', reverse,5' GACCGCCCTCTA CACCCT 3'; *Ndufb2* forward, 5' CGGGACTCGGGGAAGTGA 3', reverse,5' CTGGACCCGTCT TGTCTCTG 3'; *Ndufb8* forward, 5' CACTCACCCCATGCCATCAT 3', reverse,5' CAGAGTGA ACCGCGGAGAAG 3'; *Cox5*, forward, 5' GCGTTGTTAGACTCCCACCA 3', reverse, 5'CCACT CCGCGAAGTAACCTT 3'; *Ndufb4* forward, 5' GGGGTCGTTGTACTGAAGCA3', reverse,5' GC ACTTCCTGAGCCTGAAGG 3'; *Uqcrq* forward, 5' GTCTTTCAGAGGCAGGGGAC 3', reverse,5' GCAACCAGGAGTTTGAGCAG 3'. Percent input was calculated using the ΔΔC(t) method[81].

Statistics and reproducibility

The number of replicates for each experiment, as well as the numbers of mice/embryos used are denoted in figure legends. Unless stated otherwise, data are expressed as mean ± standard error of the mean. One-tailed Student's t-test was used for comparisons of two groups and one-way ANOVA followed by post-hoc Dunnett's test was used for multiple group comparisons tests. $P < 0.05$ were considered statistically significant and the following statistical significance indicators are used: ns denotes not significant, *$P < 0.05$; **$P < 0.005$.

Reporting summary

Further information on research design is available in the Nature Portfolio Reporting Summary linked to this article.

Data availability

Source data for all graphs and charts are provided in the figshare repository, https://doi.org/10.6084/m9.figshare.26455591.v1. NanoString data can be accessed through the NCBI Gene Express Omnibus repository with the accession number: GSE279295. Model figure created in BioRender. Kwong, J. (2023) BioRender.com/p34q043. Any remaining information can be obtained from the corresponding author upon request.

References

1. Patterson, A. J. & Zhang, L. Hypoxia and fetal heart development. *Curr. Mol. Med.* **10**, 653–666 (2010).
2. Vempati, U. D., Torraco, A. & Moraes, C. T. Mouse models of oxidative phosphorylation dysfunction and disease. *Methods* **46**, 241–247 (2008).
3. Piruat, J. I., Pintado, C. O., Ortega-Saenz, P., Roche, M. & Lopez-Barneo, J. The mitochondrial SDHD gene is required for early embryogenesis, and its partial deficiency results in persistent carotid body glomus cell activation with full responsiveness to hypoxia. *Mol. Cell Biol.* **24**, 10933–10940 (2004).
4. Li, K. et al. Cytochrome c deficiency causes embryonic lethality and attenuates stress-induced apoptosis. *Cell* **101**, 389–399 (2000).
5. Larsson, N. G. et al. Mitochondrial transcription factor A is necessary for mtDNA maintenance and embryogenesis in mice. *Nat. Genet.* **18**, 231–236 (1998).
6. Hance, N., Ekstrand, M. I. & Trifunovic, A. Mitochondrial DNA polymerase gamma is essential for mammalian embryogenesis. *Hum. Mol. Genet.* **14**, 1775–1783 (2005).
7. Zhao, Q., Sun, Q., Zhou, L., Liu, K. & Jiao, K. Complex Regulation of Mitochondrial Function During Cardiac Development. *J. Am. Heart Assoc.* **8**, e012731 (2019).
8. Baker, C. N. & Ebert, S. Development of aerobic metabolism in utero: requirement for mitochondrial function during embryonic and foetal periods. *OA Biotechnol.* **2**, 16–22 (2013).
9. Persad, K. L. & Lopaschuk, G. D. Energy Metabolism on Mitochondrial Maturation and Its Effects on Cardiomyocyte Cell Fate. *Front. Cell Dev. Biol.* **10**, 886393 (2022).
10. Liu, Y., Chen, H. & Shou, W. Potential Common Pathogenic Pathways for the Left Ventricular Noncompaction Cardiomyopathy (LVNC). *Pediatr. Cardiol.* **39**, 1099–1106 (2018).
11. Choquet, C., Kelly, R. G. & Miquerol, L. Defects in Trabecular Development Contribute to Left Ventricular Noncompaction. *Pediatr. Cardiol.* **40**, 1331–1338 (2019).
12. Towbin, J. A. & Jefferies, J. L. Cardiomyopathies Due to Left Ventricular Noncompaction, Mitochondrial and Storage Diseases, and Inborn Errors of Metabolism. *Circ. Res* **121**, 838–854 (2017).
13. Finsterer, J. Noncompaction in Mitochondrial Disorders. *Circ. Res.* **121**, e88–e89 (2017).
14. Kunji, E. R. S., King, M. S., Ruprecht, J. J. & Thangaratnarajah, C. The SLC25 Carrier Family: Important Transport Proteins in Mitochondrial Physiology and Pathology. *Physiol. (Bethesda)* **35**, 302–327 (2020).
15. Iacobazzi, V., Lauria, G. & Palmieri, F. Organization and sequence of the human gene for the mitochondrial citrate transport protein. *DNA Seq.* **7**, 127–139 (1997).
16. Majd, H., King, M. S., Smith, A. C. & Kunji, E. R. S. Pathogenic mutations of the human mitochondrial citrate carrier SLC25A1 lead to impaired citrate export required for lipid, dolichol, ubiquinone and sterol synthesis. *Biochim Biophys. Acta Bioenerg.* **1859**, 1–7 (2018).
17. Morciano, P. et al. A conserved role for the mitochondrial citrate transporter Sea/SLC25A1 in the maintenance of chromosome integrity. *Hum. Mol. Genet.* **18**, 4180–4188 (2009).
18. Sivanand, S., Viney, I. & Wellen, K. E. Spatiotemporal Control of Acetyl-CoA Metabolism in Chromatin Regulation. *Trends Biochem Sci.* **43**, 61–74 (2018).
19. Fernandez, H. R. et al. The mitochondrial citrate carrier, SLC25A1, drives stemness and therapy resistance in non-small cell lung cancer. *Cell Death Differ.* **25**, 1239–1258 (2018).
20. Wynne, M. E. et al. APOE expression and secretion are modulated by mitochondrial dysfunction. *Elife* **12**, https://doi.org/10.7554/eLife.85779 (2023).

21. Gokhale, A. et al. Mitochondrial Proteostasis Requires Genes Encoded in a Neurodevelopmental Syndrome Locus. *J. Neurosci.* **41**, 6596–6616 (2021).

22. McDonald-McGinn, D. M. et al. 22q11.2 deletion syndrome. *Nat. Rev. Dis. Prim.* **1**, 15071 (2015).

23. Unolt, M. et al. Congenital heart diseases and cardiovascular abnormalities in 22q11.2 deletion syndrome: From well-established knowledge to new frontiers. *Am. J. Med. Genet. A* **176**, 2087–2098 (2018).

24. Gokhale, A. et al. Systems Analysis of the 22q11.2 Microdeletion Syndrome Converges on a Mitochondrial Interactome Necessary for Synapse Function and Behavior. *J. Neurosci.* **39**, 3561–3581 (2019).

25. Dickinson, M. E. et al. High-throughput discovery of novel developmental phenotypes. *Nature* **537**, 508–514 (2016).

26. Tan, M. et al. Inhibition of the mitochondrial citrate carrier, Slc25a1, reverts steatosis, glucose intolerance, and inflammation in preclinical models of NAFLD/NASH. *Cell Death Differ.* **27**, 2143–2157 (2020).

27. Geiger, T. et al. Initial quantitative proteomic map of 28 mouse tissues using the SILAC mouse. *Mol. Cell Proteom.* **12**, 1709–1722 (2013).

28. Wang, M., Herrmann, C. J., Simonovic, M., Szklarczyk, D. & von Mering, C. Version 4.0 of PaxDb: Protein abundance data, integrated across model organisms, tissues, and cell-lines. *Proteomics* **15**, 3163–3168 (2015).

29. Spielmann, N. et al. Extensive identification of genes involved in congenital and structural heart disorders and cardiomyopathy. *Nat. Cardiovasc. Res.* **1**, 157–173 (2022).

30. Nota, B. et al. Deficiency in SLC25A1, encoding the mitochondrial citrate carrier, causes combined D-2- and L-2-hydroxyglutaric aciduria. *Am. J. Hum. Genet.* **92**, 627–631 (2013).

31. Balaraju, S. et al. Congenital myasthenic syndrome with mild intellectual disability caused by a recurrent SLC25A1 variant. *Eur. J. Hum. Genet.* **28**, 373–377 (2020).

32. Alzahrani, A. Y. B., Alghamdi, L. S. A., Alghamdi, H. A. M., Hassan, A. F. & Alsehemi, M. A. Congenital Myasthenic Syndrome Associated With SLC25A1 Gene Variant: The First Reported Case in Saudi Arabia. *Cureus* **15**, e35808 (2023).

33. Du, Q., de la Morena, M. T. & van Oers, N. S. C. The Genetics and Epigenetics of 22q11.2 Deletion Syndrome. *Front. Genet.* **10**, 1365 (2019).

34. Pediatric Cardiac Genomics, C. et al. The Congenital Heart Disease Genetic Network Study: rationale, design, and early results. *Circ. Res* **112**, 698–706 (2013).

35. Hoang, T. T. et al. The Congenital Heart Disease Genetic Network Study: Cohort description. *PLoS One* **13**, e0191319 (2018).

36. Hlouschek, J., Hansel, C., Jendrossek, V. & Matschke, J. The Mitochondrial Citrate Carrier (SLC25A1) Sustains Redox Homeostasis and Mitochondrial Metabolism Supporting Radioresistance of Cancer Cells With Tolerance to Cycling Severe Hypoxia. *Front Oncol.* **8**, 170 (2018).

37. Zhou, Y. et al. Metascape provides a biologist-oriented resource for the analysis of systems-level datasets. *Nat. Commun.* **10**, 1523 (2019).

38. Glancy, B., Kim, Y., Katti, P. & Willingham, T. B. The Functional Impact of Mitochondrial Structure Across Subcellular Scales. *Front Physiol.* **11**, 541040 (2020).

39. Kondadi, A. K., Anand, R. & Reichert, A. S. Functional Interplay between Cristae Biogenesis, Mitochondrial Dynamics and Mitochondrial DNA Integrity. *Int. J. Mol. Sci.* **20**, https://doi.org/10.3390/ijms20174311 (2019).

40. Jakubke, C. et al. Cristae-dependent quality control of the mitochondrial genome. *Sci. Adv.* **7**, eabi8886 (2021).

41. Karlstadt, A. et al. CardioNet: a human metabolic network suited for the study of cardiomyocyte metabolism. *BMC Syst. Biol.* **6**, 114 (2012).

42. Consortium, E. P. An integrated encyclopedia of DNA elements in the human genome. *Nature* **489**, 57–74 (2012).

43. Luo, Y. et al. New developments on the Encyclopedia of DNA Elements (ENCODE) data portal. *Nucleic Acids Res.* **48**, D882–D889 (2020).

44. Auwerx, J., Cock, T. A. & Knouff, C. PPAR-gamma: a thrifty transcription factor. *Nucl. Recept Signal* **1**, e006 (2003).

45. Zhou, L., Wang, Z. Z., Xiao, Z. C. & Tu, L. Effects of PPAR-gamma in the Myocardium on the Development of Ventricular Septation. *Curr. Med Sci.* **40**, 313–319 (2020).

46. Johnson, D. T. et al. Tissue heterogeneity of the mammalian mitochondrial proteome. *Am. J. Physiol. Cell Physiol.* **292**, C689–C697 (2007).

47. Johnson, D. T., Harris, R. A., Blair, P. V. & Balaban, R. S. Functional consequences of mitochondrial proteome heterogeneity. *Am. J. Physiol. Cell Physiol.* **292**, C698–C707 (2007).

48. Garcia, D. & Shaw, R. J. AMPK: Mechanisms of Cellular Energy Sensing and Restoration of Metabolic Balance. *Mol. Cell* **66**, 789–800 (2017).

49. James, T. N. Apoptosis in congenital heart disease. *Coron. Artery Dis.* **8**, 599–616 (1997).

50. Feng, Q. et al. Development of heart failure and congenital septal defects in mice lacking endothelial nitric oxide synthase. *Circulation* **106**, 873–879 (2002).

51. Pexieder, T. Cell death in the morphogenesis and teratogenesis of the heart. *Adv. Anat. Embryol. Cell Biol.* **51**, 3–99 (1975).

52. Martinez-Reyes, I. & Chandel, N. S. Mitochondrial TCA cycle metabolites control physiology and disease. *Nat. Commun.* **11**, 102 (2020).

53. Wellen, K. E. et al. ATP-citrate lyase links cellular metabolism to histone acetylation. *Science* **324**, 1076–1080 (2009).

54. Stollberger, C. & Finsterer, J. Noncompaction is already known in DiGeorge anomaly from 22q11.2 deletion. *Am. J Med Genet A* **155A**, 662–663 (2011). author reply 664-665.

55. Madan, S. et al. Left ventricular non-compaction on MRI in a patient with 22q11.2 distal deletion. *Am. J. Med Genet A* **152A**, 1295–1299 (2010).

56. Merscher, S. et al. TBX1 is responsible for cardiovascular defects in velo-cardio-facial/DiGeorge syndrome. *Cell* **104**, 619–629 (2001).

57. Edvardson, S. et al. Agenesis of corpus callosum and optic nerve hypoplasia due to mutations in SLC25A1 encoding the mitochondrial citrate transporter. *J. Med Genet* **50**, 240–245 (2013).

58. Prasun, P. et al. Expanding the Clinical Spectrum of Mitochondrial Citrate Carrier (SLC25A1) Deficiency: Facial Dysmorphism in Siblings with Epileptic Encephalopathy and Combined D,L-2-Hydroxyglutaric Aciduria. *JIMD Rep.* **19**, 111–115 (2015).

59. Cohen, I. et al. A novel homozygous SLC25A1 mutation with impaired mitochondrial complex V: Possible phenotypic expansion. *Am. J. Med Genet A* **176**, 330–336 (2018).

60. Bankhead, P. et al. QuPath: Open source software for digital pathology image analysis. *Sci. Rep.* **7**, 16878 (2017).

61. Homsy, J. et al. De novo mutations in congenital heart disease with neurodevelopmental and other congenital anomalies. *Science* **350**, 1262–1266 (2015).

62. Jin, S. C. et al. Contribution of rare inherited and de novo variants in 2,871 congenital heart disease probands. *Nat. Genet* **49**, 1593–1601 (2017).

63. Zaidi, S. et al. De novo mutations in histone-modifying genes in congenital heart disease. *Nature* **498**, 220–223 (2013).

64. Van der Auwera, G. A. et al. From FastQ data to high confidence variant calls: the Genome Analysis Toolkit best practices pipeline. *Curr. Protoc. Bioinforma.* **43**, 11 10 11–11 10 33 (2013).

65. McKenna, A. et al. The Genome Analysis Toolkit: a MapReduce framework for analyzing next-generation DNA sequencing data. *Genome Res* **20**, 1297–1303 (2010).

66. Purcell, S. et al. PLINK: a tool set for whole-genome association and population-based linkage analyses. *Am. J. Hum. Genet* **81**, 559–575 (2007).
67. Yu, Z. & Deng, L. Pseudosibship methods in the case-parents design. *Stat. Med* **30**, 3236–3251 (2011).
68. Navarro Gonzalez, J. et al. The UCSC Genome Browser database: 2021 update. *Nucleic Acids Res* **49**, D1046–D1057 (2021).
69. Wang, K., Li, M. & Hakonarson, H. ANNOVAR: functional annotation of genetic variants from high-throughput sequencing data. *Nucleic Acids Res* **38**, e164 (2010).
70. Kircher, M. et al. A general framework for estimating the relative pathogenicity of human genetic variants. *Nat. Genet* **46**, 310–315 (2014).
71. Karczewski, K. J. et al. The mutational constraint spectrum quantified from variation in 141,456 humans. *Nature* **581**, 434–443 (2020).
72. Lee, S. et al. WISARD: workbench for integrated superfast association studies for related datasets. *BMC Med Genomics* **11**, 39 (2018).
73. Han, H. et al. TRRUST v2: an expanded reference database of human and mouse transcriptional regulatory interactions. *Nucleic Acids Res* **46**, D380–D386 (2018).
74. Picard, M., White, K. & Turnbull, D. M. Mitochondrial morphology, topology, and membrane interactions in skeletal muscle: a quantitative three-dimensional electron microscopy study. *J. Appl Physiol. (1985)* **114**, 161–171 (2013).
75. Jha, P., Wang, X. & Auwerx, J. Analysis of Mitochondrial Respiratory Chain Supercomplexes Using Blue Native Polyacrylamide Gel Electrophoresis (BN-PAGE). *Curr. Protoc. Mouse Biol.* **6**, 1–14 (2016).
76. Beutner, G., Eliseev, R. A. & Porter, G. A. Jr. Initiation of electron transport chain activity in the embryonic heart coincides with the activation of mitochondrial complex 1 and the formation of supercomplexes. *PLoS One* **9**, e113330 (2014).
77. Ghazal, N., Peoples, J. N., Mohiuddin, T. A. & Kwong, J. Q. Mitochondrial functional resilience after TFAM ablation in the adult heart. *Am. J. Physiol. Cell Physiol.* **320**, C929–C942 (2021).
78. Karlstaedt, A. et al. Oncometabolite d-2-hydroxyglutarate impairs alpha-ketoglutarate dehydrogenase and contractile function in rodent heart. *Proc. Natl Acad. Sci. USA* **113**, 10436–10441 (2016).
79. Aksentijevic, D. et al. Cardiac dysfunction and peri-weaning mortality in malonyl-coenzyme A decarboxylase (MCD) knockout mice as a consequence of restricting substrate plasticity. *J. Mol. Cell Cardiol.* **75**, 76–87 (2014).
80. Gurobi Optimization, L. Gurobi Optimizer Reference Manual. (2023).
81. Lin, X., Tirichine, L. & Bowler, C. Protocol: Chromatin immunoprecipitation (ChIP) methodology to investigate histone modifications in two model diatom species. *Plant Methods* **8**, 48 (2012).

Acknowledgements

Author contributions
J.Q.K. and C.O. wrote the manuscript. J.N.P., C.O., N.G., A.G., F.S., J.T.G., M.E.B., and J.Q.K. performed experiments. A.K. conducted computational flux analysis and CardioNet modeling. J.Q.K., V.F., A.K., M.E.D., J.N.P., C.O., J.T.G., and G.A.P. analyzed the data. J.Q.K., J.N.P., and C.O. designed the study. J.Q.K. conducted experimental oversight.

Competing interests
The authors declare no competing interests.

Additional information
Supplementary information The online version contains supplementary material available at https://doi.org/10.1038/s42003-024-07110-8.

Correspondence and requests for materials should be addressed to Jennifer Q. Kwong.

Peer review information *Communications Biology* thanks Carrie Welch and the other, anonymous, reviewer(s) for their contribution to the peer review of this work. Primary Handling Editor: Dario Ummarino.

Reprints and permissions information is available at http://www.nature.com/reprints

Publisher's note Springer Nature remains neutral with regard to jurisdictional claims in published maps and institutional affiliations.